1   Circulation-driven variability of Atlantic anthropogenic carbon transports and uptake

2

3   Peter J. Brown[1*], Elaine L. McDonagh[1,2], Richard Sanders[1,2], Andrew J. Watson[3], Rik

4   Wanninkhof[4], Brian A. King[1], David A. Smeed[1], Molly O. Baringer[4], Christopher S. Meinen[4],

5   Ute Schuster[3], Andrew Yool[1], Marie-José Messias[3].

6

7   1. National Oceanography Centre, Southampton, UK

8   2. NORCE, Norwegian Research Centre, Bjerknes Centre for Climate Research, Bergen,

9   Norway

10   3. College of Life and Environmental Sciences, University of Exeter, Exeter, UK

11   4. NOAA / Atlantic Oceanographic and Meteorological Laboratory, Miami, Florida, USA

12

13   **The ocean absorbs approximately a quarter of the carbon dioxide currently released to the**

14   **atmosphere by human activities (C_{anth}). A disproportionately large fraction accumulates in**

15   **the North Atlantic due to the combined effects of transport by the Atlantic Meridional**

16   **Overturning Circulation (AMOC) and air-sea exchange. However, discrepancies exist**

17   **between modelled and observed estimates of the air-sea exchange due to unresolved ocean**

18   **transport variability. Here we quantify the strength and variability of C_{anth} transports**

19   **across 26.5°N in the North Atlantic between 2004 and 2012 using circulation measurements**

20   **from the RAPID mooring array and hydrographic observations. Over this time period,**

21   **decreasing circulation strength tended to decrease northward C_{anth} transport, while**

22   **increasing C_{anth} concentrations (preferentially in the upper limb of the overturning**

23   **circulation) tended to increase northward C_{anth} transport. These two processes**

24   **compensated each other over the 8.5-year period. While ocean transport and air-sea C_{anth}**

25   **fluxes are approximately equal in magnitude, the increasing accumulation rate of C_{anth} in**

26   **the North Atlantic combined with a stable ocean transport supply means we infer a**

27   **growing contribution from air-sea C_{anth} fluxes over the time period. North Atlantic C_{anth}**

28   **accumulation is thus sensitive to AMOC strength, but growing atmospheric C_{anth} uptake**

29   **continues to significantly impact C_{anth} transports.**

30   The ocean exchanges carbon dioxide (CO_2) rapidly with the atmosphere, with regions of

31   substantial net CO_2 uptake and release created by ocean circulation, biological processes and

32   heat and freshwater fluxes[1]. In pre-industrial times the global net CO_2 flux from the ocean to the

33   atmosphere is estimated to have been ~0.45-0.78 PgC yr^{-1} balancing riverine carbon inputs[2,3].

34   However, increasing atmospheric CO_2 concentrations since the beginning of the Industrial

35   Revolution have reversed the flux, transferring anthropogenic carbon (C_{anth}) into the ocean at a

36   rate of 2.6 ± 0.3 PgC yr^{-1} [4], slowing the accumulation of anthropogenic CO_2 in the atmosphere

37   and reducing the pace of global warming. This net global oceanic C_{anth} uptake accounts for

38   nearly 50% of all historical fossil fuel emissions[5] and 23% of total contemporary emissions[6].

39   Understanding the processes that cause this uptake to occur and their susceptibility to change are

40   therefore high priority activities.

41   The North Atlantic (NA) and Arctic region (from the Equator to Bering Strait) is a key region as

42   it plays a disproportionately large role in the uptake of both CO_2 and C_{anth} from the atmosphere.

43   It was a regional sink for atmospheric carbon in pre-industrial times[7], and now accounts for

44   approximately 25% of all contemporary global CO_2 uptake from the atmosphere[6,8] and 25% of

45   the global ocean C_{anth} inventory[4,5,9,10] despite having only 15% of the global ocean surface. The

46   "natural" (pre-industrial) CO_2 uptake results from both the surface cooling of warm water

47   advected polewards prior to sinking, as part of the Atlantic Meridional Overturning Circulation

48   (AMOC, see Figure 1, adapted from [11]), and from strong biological production[12]. The AMOC

49   generates a net southward transport of contemporary (natural and anthropogenic) carbon, with

50   lower carbon concentrations in the warm, upper northward flow being exceeded by higher

51   concentrations in the cold, deep return flow[7,13]. Conversely, the post-industrial build-up of C_{anth}

52   in surface waters generates a surface-enhanced concentration profile (Figure 1 for C_{anth}

53   distribution along 26.5°N); when combined with the action of the overturning circulation this

54   leads to a net northward transport of C_{anth} into the NA[13,14], the opposite direction to the natural

55   carbon transport and contributes to the highest regional C_{anth} accumulation rates in the global

56   ocean[4,5].

57   The size, variability and controls of the ocean circulation contribution to regional C_{anth} storage

58   and hence the resilience of this sink to global change are largely unknown. Prior observational

59   estimates of NA C_{anth} accumulation, from individual synoptic repeat hydrographic sections, vary

60   widely (0.19-0.43 PgC yr^{-1} [13–17], Table 1), with more constrained estimates possible only through

61   larger-scale, regional/global analyses (0.38-0.47 PgC yr^{-1}, from ocean inversion and data

62   assimilation models or observational integrations[4,10,18]). Cruise-based estimates of northward

63   ocean C_{anth} transports meanwhile (0.17-0.25 PgC yr^{-1} [13–17]) are typically much higher than

64   estimates from biogeochemical models, ocean inversions and data assimilations (0.09-0.15 PgC

65   yr^{-1} [4,10,18–20]); this is primarily due to cruise-based C_{anth} transport estimates being based on single

66   "snapshot" estimates of ocean circulation (principally the AMOC), and the inability of

67   biogeochemical models and data assimilations to correctly estimate volume transports[19].

68   Between 27% and 66% of C_{anth} accumulation is thus driven by the northward ocean transport

69   (the remainder being taken up from the atmosphere). The magnitude of the range is indicative of

70   the uncertainty related to unresolved temporal variability, observational and methodological

71   limitations, and that each estimate is associated with a single state of the circulation or AMOC

72   strength.

73   It is now clear that individual snapshot estimates of AMOC strength used in previous

74   calculations of C_{anth} uptake (variability of which is removed by the inversion/ assimilation

75   techniques described above) do not fully capture true circulation variability[21]. The AMOC

76   estimated from the RAPID-MOCHA-WBTS programme at 26.5°N[21] (Figure 1) had an average

77   strength of 17.2 Sv over the 2004-2012 period, with substantial temporal variability (10 day

78   filtered root mean square variability of 4.6 Sv, variability of annual means of 2.2 Sv)[21,22].

79   However this variability was superimposed on a significant decreasing trend in AMOC

80   magnitude of -0.54 Sv yr^{-1} which occurred over the same time period[23,24]. CMIP5 Earth System

81   models have predicted that weakening of AMOC strength similar in scale to this recently

82   observed will lead to a decline in both surface CO_2 uptake and accumulation at depth as climate

83   change feedbacks strengthen[25].

84   **High frequency anthropogenic carbon transport estimates**

85   In this article we investigate the impact of observed circulation change on C_{anth} accumulation in

86   the NA between 2004 and 2012 , combining ten-day AMOC transport fields at 26.5°N[21,26] with

87   C_{anth} concentrations estimates. A time series of C_{anth} concentration distributions is generated

88   using regressions constructed from all available hydrographic data at 26.5°N and applied to the

89   RAPID-Argo ten-day temperature-salinity fields[26] (see Methods, Extended Data Figures 1-3,

90   Extended Data Table 1). Therefore, it includes variability associated with the changing

91   distribution of water masses on the section (from RAPID and Argo) and longer-term, water

92   mass-specific concentration trends (from repeat hydrography). In addition, in the upper 200m of

93   the water column we incorporate a new Scaled Pre-industrial DisEquilibrium (SPIDEr) method

94   based on sea-surface pCO_2 observations to account for seasonal variation of the C_{anth}

95   concentration that has not been included in previous treatments[15]; this ensures feasible year-

96   round concentration ranges that are consistent with Revelle factor (Rf) variability and air-sea

97   fluxes (Methods, Extended Data Figures 4-5). For the region east of the Bahamas, estimated C_{anth}

98   distributions are combined with ten-day mooring/float derived transport fields, while in Florida

99   Straits we calculate a transport-weighted C_{anth} (C_{anth} transport divided by volume transport) time

100 series from repeat hydrographic sections that enables combination with the submarine cable-

101 derived transport time series (Methods, Extended Data Figure 6).   Uncertainties in C_{anth}

102 transports were calculated following the approach used for freshwater transport[26] but also

103 accounting for uncertainties associated with C_{anth} estimation and trends (Methods, Extended Data

104 Table 2). The uncertainty in volume transport contributes 70% to the total error estimate, with

105 uncertainties relating to the C_{anth} concentrations contributing approximately 30%. We analysed

106 the robustness and appropriateness of the methodology employed for estimating C_{anth} and its

107 transport for the time between hydrographic sections by using model outputs. Predicted C_{anth}

108 transport fields (generated as for observations, using predictive parameterisations of model

109 'truth' C_{anth}) were compared with explicitly determined model C_{anth} transport fields (based on

110 parallel NEMO-MEDUSA 1° model runs with and without atmospheric CO_2 growth and with

111 identical physical fields), and suggested the approach can reproduce the 2004-2012 model mean

112 to within 3% of the model truth, and shorter-term estimates (1 month) to within ~9% (worst-

113 case) (Methods, Extended Data Figure 7). Finally, we tested the back-calculation C_{anth} estimation

114 method employed on hydrographic data by direct application to model outputs; results showed

115   accuracy to within 0.5% for the 2004-2012 C_{anth} transport model mean and to within ~7% for

116   shorter, 1-month estimates (Methods, Extended Data Figure 8).

Circulation components of anthropogenic carbon transport

118   Figure 2 summarizes the transport of C_{anth} across the 26.5°N section. A mean northwards C_{anth}

119   transport is calculated for 2004-2012 of 0.191 ± 0.013 PgC yr^{-1} (mean ± total uncertainty in time

120   series mean, Fig. 2a black line, Extended Data Table 2, Methods). This lies within the range of

121   previous estimates determined from hydrography but is larger than that derived from inversion

122   models (Table 1). The mean net C_{anth} transport is largely set by the difference between the

123   northward Florida Straits transport and the southward interior transport between 0 and 1,100 db,

124   the two largest transport components (Fig. 2a, Table 2). Although the mean volume transport in

125   the Florida Straits (31.6 Sv) is greater than the geostrophic interior transport (-18.6 Sv) the

126   transport-weighted C_{anth} for the interior (65.6 µmol kg^{-1}) is higher than that for Florida Straits

127   (54.4 µmol kg^{-1}), reflective of the accumulation of C_{anth} in surface waters as they recirculate in

128   the anticyclonic gyre from the western boundary (Fig. 1). Contributions from northward Ekman

129   C_{anth} transports (3.5 Sv, driven by surface winds and calculated from ERA-Interim data) enhance

130   the net total C_{anth} transport, and show strong variability and occasional southward incursions.

131   While the combined transports between 1,100 and 5,000 db (-18.7 Sv) make up the smallest

132   contribution to the overall C_{anth} transport (southward export of 0.09 PgC yr^{-1}, transport-weighted

133   C_{anth} 12.5 µmol kg^{-1}, Table 2, Fig. 2a), they do represent the NA's input to long-term storage of

134   carbon in the deep ocean, equivalent to 4% of the total annual global C_{anth} uptake rate[4].

135   There is a high degree of variability over the 8.5-year record, with a maximum annual peak-to-

136   peak amplitude of 0.48 PgC yr^{-1} (December 2008 to December 2009, Fig. 2a,d), a standard

137   deviation of ten-day transport estimates of 0.08 PgC yr^{-1} and substantial interannual variability

138   with annual means ranging from 0.11 to 0.23 PgC yr^{-1} (Fig. 2b). Application of a three-month

139   low-pass filter reveals a strong seasonal cycle (amplitude 0.08 PgC yr^{-1}, Fig. 2c).

140   Following methods used for freshwater[26] we additionally separated C_{anth} transport into

141   overturning, horizontal and throughflow components (Fig. 2d) as an indication of the dominant

142   components of C_{anth} transport strength and variability: overturning describes the transport's

143   vertical structure (zonally-averaged C_{anth} and velocity fields with the section average removed),

144   horizontal represents the gyre and eddy transports (calculated as the total C_{anth} transport with

145   mean and overturning contributions removed), and throughflow represents the ~0.8 Sv of Pacific

146   water that flows southwards through the Atlantic from Bering Strait (see Methods for details).

147   The throughflow component is almost zero for C_{anth} (-0.8 TgC yr^{-1}, 1000 Tg=1Pg) as per

148   previous studies[13,15] and is not shown. The overturning C_{anth} transport is northwards (mean ±

149   standard deviation: +0.31 ± 0.09 PgC yr^{-1}), its sign representative of the upper ocean northward

150   limb having higher C_{anth} concentrations than its deep, southward-flowing limb (Fig. 1, Table 2).

151   The horizontal C_{anth} transport is southwards (mean ± standard deviation: -0.11 ± 0.02 PgC yr^{-1})

152   and derives from the west-east C_{anth} concentration gradient combining with both the north- and

153   southward gyre and eddy transports, and the horizontal component of the Florida Straits transport

154   being compensated by southward flow in the upper ocean of the interior east of the Bahamas.

155   The horizontal C_{anth} transport component is smaller in magnitude and less variable than the

156   overturning component (Fig. 2d), with AMOC volume transport variability describing 80% of

157   the variance in C_{anth} transports. This strong AMOC:C_{anth} transport correlation at 26.5°N (Fig. 3a)

158   is supported by model outputs[19] and here indicates a 1 Sv increase in overturning is associated

159   with an 18 TgC yr^{-1} increase in C_{anth} transport. There is temporal structure in the correlation's

160   residual (Fig. 3b) with the residual growing over the length of the time series; this represents that

7

161   part of the variability that is not correlated with the AMOC (such as increasing C_{anth} loadings)

162   and can be interpreted as an increase in the sensitivity of C_{anth} transports per Sverdrup of AMOC.

163   Despite increasing C_{anth} concentrations there is no trend in the total C_{anth} transport across 26.5°N

164   between 2004 and 2012. Significant trends are, however, present in the subregions, with the

165   largest (and near-compensating) trends associated with the two largest components (positive

166   trend, Florida Straits; negative trend, upper mid-ocean, Table 2). Although the C_{anth} transport-

167   AMOC correlation and a decrease in AMOC strength of -0.54 Sv yr^{-1} observed between 2004-

168   2012[23] predicts a decreasing overturning component trend (-10 TgC yr^{-2}), the observed value is

169   much smaller (-6 TgC yr^{-2}) due to increasing C_{anth} concentrations. The overturning trend is not

170   replicated in the total C_{anth} transport trend (-0.4 TgC yr^{-2}) due to a compensating trend in the

171   horizontal gyre component (+5 TgC yr^{-2}).

172   **Circulation change and water column C_{anth} accumulation**

173   We can separate the impact of circulation change and water column C_{anth} accumulation on total

174   and component C_{anth} transports by removing water-mass-specific C_{anth} trends from the predicted

175   C_{anth} fields and recombining the residual with the volume transport estimates. The time series

176   generated represents the effect of volume-transport trends on an unchanging C_{anth} field while the

177   difference from the full transport time series reflects the effect of additional C_{anth} load (Fig. 4 and

178   Table 2). For the total northwards C_{anth} transport, this shows that circulation changes cause a

179   decline of 94 TgC yr^{-1} over 8.5 years.

180   However, this is balanced by an increasing transport due to growing C_{anth} concentrations derived

181   from air-sea exchange of 89 TgC yr^{-1}. Together they generate a total C_{anth} transport with no

182   significant trend, thus implying that for 2004-2012 C_{anth} increases are counter balanced by the

183   effect of circulation change on the total oceanic supply of C_{anth} to the NA. For individual C_{anth}

184 transport components and subregions, the Florida Straits and the upper ocean interior still

185 dominate; the increasing northward trend in Florida Straits is driven by growing C_{anth} loads (19

186 TgC yr^{-1}); the increasingly southward (negative) interior trend is approximately one-third due to

187 increasing C_{anth} concentrations (-6 TgC yr^{-1}) and approximately two-thirds due to volume

188 transport decreases (-12 TgC yr^{-1}).

189 The horizontal C_{anth} transport is increasing (becoming more northward) because the Florida

190 Straits transport-weighted C_{anth} trend is larger than the trend in the interior. The difference in the

191 trends is due to C_{anth} concentrations increasing faster at the western boundary than at the eastern

192 boundary, thereby diminishing the west-to-east gradient (Fig. 1). The decreasing trend in

193 overturning volume transport over the period is produced by balancing increases in southward

194 moving upper waters (-0.48 Sv yr^{-1}) and reductions in southward-moving deep waters (between

195 3,000 and 5,000 db; +0.48 Sv yr^{-1}). This then creates an associated reduction in the northward

196 C_{anth} overturning transport.

197 **The NA C_{anth} budget**

198 For the NA and Arctic region (26.5°N to Bering Strait), a regional C_{anth} budget of ocean

199 transport, storage and air-sea fluxes can be formed using a storage rate of 0.39-0.47 PgC yr^{-1} for

200 2004[10,15,18]. Combining our derived northward transport across 26.5°N of 0.191 PgC yr^{-1} with the

201 total C_{anth} contribution through the Bering Strait (0.008 PgC yr^{-1})[15], suggests that lateral oceanic

202 transport supplies between 42% and 51% of the C_{anth} accumulating in the NA and Arctic. The

203 remainder of the storage term must then originate from air-sea uptake (0.19-0.27 PgC yr^{-1}).

204 The dominant air-sea flux contribution calculated here compares well with estimates from ocean

205 inversions[18] and ocean assimilations[10] for the same timeframe (0.28-0.35 PgC yr^{-1}, Table 1),

206 despite ocean C_{anth} transport estimates differing somewhat. However, it differs markedly from

207   the only previous estimate from observations where ocean transport dominates and air-sea uptake

208   supplies only 0.13 PgC yr^{-1} (33%) to C_{anth} inventory growth for 2004[15]. This difference comes

209   largely from our revised estimate of the ocean transport term that, as the time series and our

210   seasonal correction to the near-surface concentrations show, exhibits large seasonal and

211   interannual variability which have not previously been taken into consideration and are aliased in

212   hydrographic-only transport estimates.

213   Contemporary sea-to-air CO_2 flux estimates calculated using sea surface ΔpCO_2 observations

214   suggest an annual uptake for the NA-Arctic region north of 14-18°N of -0.53-0.63 PgC yr^{-1} for

215   2004[27,28] (regional extents differ somewhat from ours, due to the choice of latitudinal boundaries

216   by previous studies). Our C_{anth} uptake estimate of -0.19-0.27 PgC yr^{-1} constitutes 40% of this

217   signal, with the remainder (mean ± range -0.35 ± 0.08 PgC yr^{-1}) being the "natural" uptake that

218   would also have existed pre-industrially, a value consistent with global inverse model outputs

219   (natural air-sea CO_2 flux neglecting riverine contribution -0.33 ± 0.08 PgC yr^{-1}, and C_{anth} air-sea

220   flux -0.31 ± 0.08 PgC yr^{-1} scaled to 2004)[18,29]. Our revised estimate for the C_{anth} transport into

221   the region provides consistency between observational and model estimates of the anthropogenic

222   and pre-industrial components of the NA's uptake of atmospheric CO_2.

223   The results presented here establish a strong relationship between the strength of the Atlantic

224   overturning circulation and the oceanic contribution to the growing NA C_{anth} inventory (as

225   inferred from rising air-sea CO_2 uptake[28,30] and historical storage increases[31]), confirming the

226   recent outputs of a biogeochemical model[19]. The northward C_{anth} transport is highly variable on

227   both short (10 day) and annual time periods, but when averaged over a nearly decadal period it

228   shows no significant trend. Although as regional C_{anth} accumulation continues to increase[4], this

229   implies a decrease in the relative contribution from northward ocean C_{anth} transport. This result

230 places greater emphasis on air-sea fluxes as the means by which local C_{anth} storage rates are

231 maintained.

232 The overturning circulation is still the primary conduit in the NA by which CO_2 is both absorbed

233 from the atmosphere (the AMOC-related transport and fluxes of heat and nutrients drive the

234 strength of both physical and biological carbon pumps) and C_{anth}-rich waters are isolated from

235 the surface on extended timescales[12,32]. While the long-term NA carbon sink is currently thought

236 to be tracking the atmospheric CO_2 increase[30], surface warming is beginning to affect the uptake

237 capacity of the subtropics[33]. This change combined with predicted long-term changes in AMOC

238 strength[34] and buffering capacity[35] imparts substantial uncertainty to the future behaviour of the

239 NA carbon sink over the twenty-first century[20,25] and its ability to slow atmospheric CO_2 increase

240 rates.

241

242 ONLINE CONTENT

243 Methods, along with any additional Extended Data display items and Source Data, are available

244 in the online version of the paper; references unique to these sections appear only in the online

245 paper

246

247 REFERENCES

248 1. Sarmiento, J. L. & Gruber, N. Carbon Cycle, CO_2, and Climate. in *Ocean Biogeochemical*

249   *Dynamics* 392–457 (Princeton Univ. Press Princeton, NJ, 2006).

250 2. Jacobson, A. R., Fletcher, S. E. M., Gruber, N., Sarmiento, J. L. & Gloor, M. A joint

251   atmosphere-ocean inversion for surface fluxes of carbon dioxide: 1. Methods and global-

252   scale fluxes. *Global Biogeochem. Cycles* **21**, (2007).

253   3.   Resplandy, L. *et al.* Revision of global carbon fluxes based on a reassessment of oceanic

254   and riverine carbon transport. *Nat. Geosci.* **11**, 504–509 (2018).

255   4.   Gruber, N. *et al.* The oceanic sink for anthropogenic CO 2 from 1994 to 2007. *Science*

256   *(80-.)*. **363**, 1193–1199 (2019).

257   5.   Sabine, C. L. *et al.* The Oceanic Sink for Anthropogenic CO2. *Science (80-.).* **305**, 367

258   LP – 371 (2004).

259   6.   Friedlingstein, P. *et al.* Global Carbon Budget 2019. *Earth Syst. Sci. Data* **11**, 1783–1838

260   (2019).

261   7.   Broecker, W. S. & Peng, T. H. Interhemispheric transport of carbon dioxide by ocean

262   circulation. *Nature* **356**, 587–589 (1992).

263   8.   Landschützer, P., Gruber, N. & Bakker, D. C. E. *An observation-based global monthly*

264   *gridded sea surface pCO2 and air-sea CO2 flux product from 1982 onward and its*

265   *monthly climatology (NCEI Accession 0160558), Version 5.5.* (2020).

266   9.   Khatiwala, S. *et al.* Global ocean storage of anthropogenic carbon. *Biogeosciences* **10**,

267   2169–2191 (2013).

268   10.   Devries, T. The oceanic anthropogenic CO2 sink: Storage, air-sea fluxes, and transports

269   over the industrial era. *Global Biogeochem. Cycles* **28**, 631–647 (2014).

270   11.   Srokosz, M. a. & Bryden, H. L. Observing the Atlantic Meridional Overturning

271   Circulation yields a decade of inevitable surprises. *Science (80-.).* **348**, 1255575–1255575

272   (2015).

273   12.   Sarmiento, J., Gruber, N., Brzezinski, M. & Dunne, J. High-latitude controls of

274   thermocline nutrients and low latitude biological productivity. *Nature* **427**, 56–60 (2004).

275   13.   Macdonald, A. M., Baringer, M. O., Wanninkhof, R., Lee, K. & Wallace, D. W. R. A

276 1998–1992 comparison of inorganic carbon and its transport across 24.5°N in the Atlantic.

277 *Deep Sea Res. Part II Top. Stud. Oceanogr.* **50**, 3041–3064 (2003).

278 14. Rosón, G., Ríos, A. F., Pérez, F. F., Lavín, A. M. & Bryden, H. L. Carbon distribution,

279 fluxes, and budgets in the subtropical North Atlantic Ocean (24.5°N). *J. Geophys. Res.*

280 **108**, 3144 (2003).

281 15. Pérez, F. F. *et al.* Atlantic Ocean CO2 uptake reduced by weakening of the meridional

282 overturning circulation. *Nat. Geosci.* **6**, 146–152 (2013).

283 16. Álvarez, M., Ríos, A. F., Pérez, F. F., Bryden, H. L. & Rosón, G. Transports and budgets

284 of total inorganic carbon in the subpolar and temperate North Atlantic. *Global*

285 *Biogeochem. Cycles* **17**, 2-1-2–21 (2003).

286 17. Zunino, P. *et al.* Transports and budgets of anthropogenic CO 2 in the tropical North

287 Atlantic in 1992-1993 and 2010-2011. *Global Biogeochem. Cycles* **29**, 1075–1091 (2015).

288 18. Mikaloff Fletcher, S. E. *et al.* Inverse estimates of anthropogenic CO 2 uptake, transport,

289 and storage by the ocean. *Global Biogeochem. Cycles* **20**, n/a-n/a (2006).

290 19. Racapé, V. *et al.* Transport and storage of anthropogenic C in the North Atlantic Subpolar

291 Ocean. *Biogeosciences* **15**, 4661–4682 (2018).

292 20. Tjiputra, J. F., Assmann, K. & Heinze, C. Anthropogenic carbon dynamics in the

293 changing ocean. *Ocean Sci.* **6**, 605–614 (2010).

294 21. McCarthy, G. D. *et al.* Measuring the Atlantic Meridional Overturning Circulation at

295 26°N. *Prog. Oceanogr.* **130**, 91–111 (2015).

296 22. Cunningham, S. A. *et al.* Temporal variability of the Atlantic meridional overturning

297 circulation at 26.5°N. *Science (80-.).* **317**, 935–938 (2007).

298 23. Smeed, D. A. *et al.* Observed decline of the Atlantic meridional overturning circulation

299   2004-2012. *Ocean Sci.* **10**, 29–38 (2014).

300   24.   Smeed, D. A. *et al.* The North Atlantic Ocean Is in a State of Reduced Overturning.

301   *Geophys. Res. Lett.* **45**, 1527–1533 (2018).

302   25.   Schwinger, J. *et al.* Nonlinearity of Ocean Carbon Cycle Feedbacks in CMIP5 Earth

303   System Models. *J. Clim.* **27**, 3869–3888 (2014).

304   26.   McDonagh, E. L. *et al.* Continuous Estimate of Atlantic Oceanic Freshwater Flux at

305   26.5°N. *J. Clim.* **28**, 8888–8906 (2015).

306   27.   Takahashi, T. *et al.* Climatological mean and decadal change in surface ocean pCO2, and

307   net sea-air CO2 flux over the global oceans. *Deep Sea Res. Part II Top. Stud. Oceanogr.*

308   **56**, 554–577 (2009).

309   28.   Schuster, U. *et al.* An assessment of the Atlantic and Arctic sea–air CO_2 fluxes, 1990–

310   2009. *Biogeosciences* **10**, 607–627 (2013).

311   29.   Gruber, N. *et al.* Oceanic sources, sinks, and transport of atmospheric CO 2. *Glob.*

312   *Biogeochem. Cycles* **23**, GB1005 (2009).

313   30.   Mckinley, G. A., Fay, A. R., Takahashi, T. & Metzl, N. Convergence of atmospheric and

314   North Atlantic carbon dioxide trends on multidecadal timescales. *Nat. Geosci.* **4**, 606–610

315   (2011).

316   31.   Woosley, R. J., Millero, F. J. & Wanninkhof, R. Rapid anthropogenic changes in CO 2

317   and pH in the Atlantic Ocean: 2003-2014. *Global Biogeochem. Cycles* **30**, 70–90 (2016).

318   32.   Steinfeldt, R., Rhein, M., Bullister, J. & Tanhua, T. Inventory changes in anthropogenic

319   carbon from 1997–2003 in the Atlantic Ocean between 20°S and 65°N. *Global*

320   *Biogeochem. Cycles* **23**, 1–11 (2009).

321   33.   Fay, A. R. & McKinley, G. A. Global trends in surface oceanpCO2from in situ data.

322   *Global Biogeochem. Cycles* **27**, 541–557 (2013).

323   34.   Cheng, W., Chiang, J. C. H. & Zhang, D. Atlantic Meridional Overturning Circulation

324   (AMOC) in CMIP5 Models: RCP and Historical Simulations. *J. Clim.* **26**, 7187–7197

325   (2013).

326   35.   Halloran, P. R. *et al.* The mechanisms of North Atlantic CO2 uptake in a large Earth

327   System Model ensemble. *Biogeosciences* **12**, 4497–4508 (2015).

328

329   CORRESPONDING AUTHOR

330   All correspondence and requests for materials should be addressed to P.J.B.

331   (peter.brown@noc.ac.uk)

332
333
334   ACKNOWLEDGEMENTS

342

343   AUTHOR CONTRIBUTIONS

344   E.L.M., B.A.K, R.S. and A.J.W designed the study. P.J.B performed the analysis. P.J.B., E.L.M.,

345   R.S. and A.J.W wrote the manuscript. D.S., U.S., M.O.B., C.S.M. and R.W. gave technical

346   support and conceptual advice. M.O.B., C.S.M., A.Y., U.S. & M.-J.M. contributed observational

347   data.

348

349   COMPETING INTERESTS

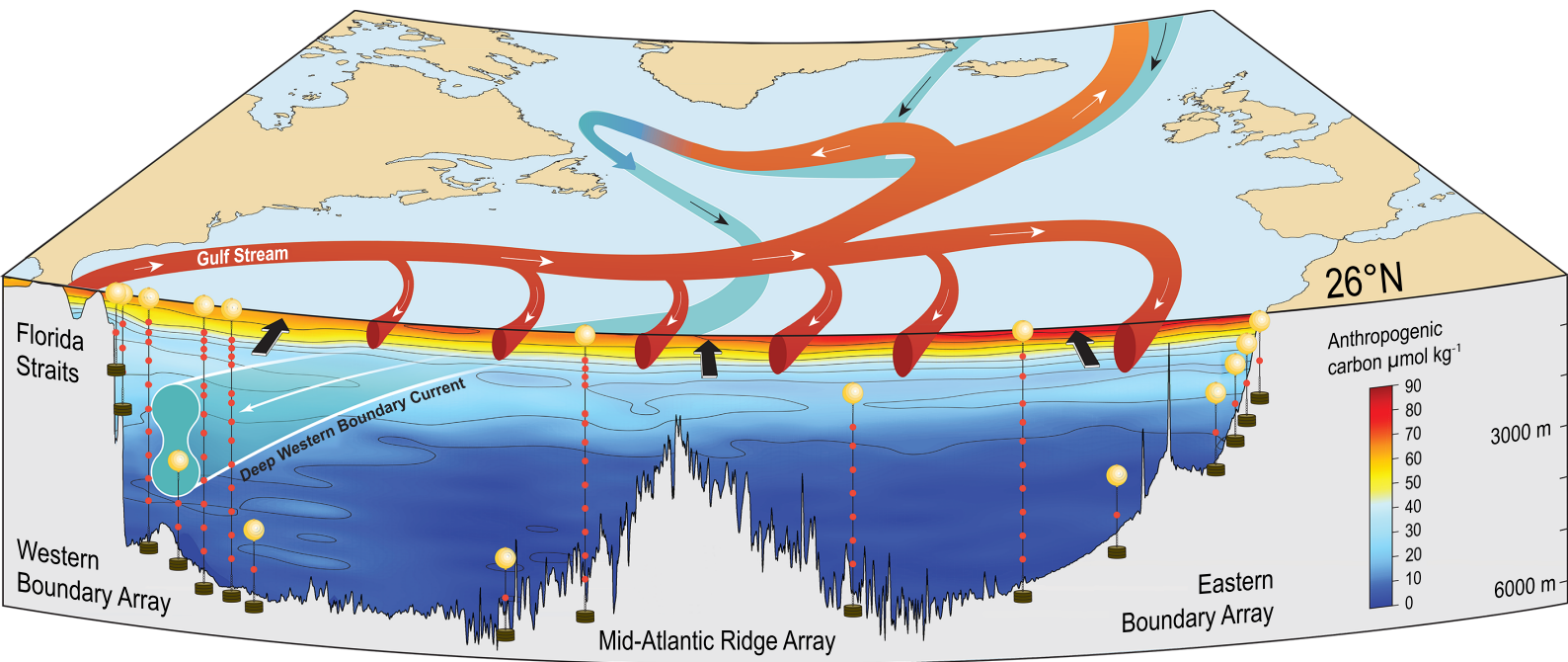350   The authors declare no competing interests.

351

352

353

354   FIGURES

355   Figure 1. AMOC observing system mooring array at 26.5°N with 2010 anthropogenic carbon

356   distribution. Ekman transport is represented by black arrows, warm water circulation in the top

357   1,100 m is represented by white arrows on red, and black and white arrows on teal represent the

358   mainly southward flow of colder, deeper waters. Adapted from [11] – reprinted with permission

359   from AAAS.

360

361

Florida Straits

Western Boundary Array

Gulf Stream

Deep Western Boundary Current

Mid-Atlantic Ridge Array

Eastern Boundary Array

26°N

Anthropogenic carbon µmol kg⁻¹

90
80
70
60
50
40
30
20
10
0

3000 m

6000 m

362   Figure 2. C_{anth} transports across 26.5°N in the subtropical NA. (a) Ten-day and three month low-

363   pass (bold) time series of C_{anth} transports in (from top to bottom): Florida Straits Gulf Stream

364   (red), total transport (black), Ekman layer (blue), waters between 3,000 and 5,000 m (grey),

365   waters between 1,100 and 3,000 m (yellow), and waters shallower then 1,100 m (pink-magenta)

366   from April 2004 to October 2012. (b) Annual averages and standard error of the mean of C_{anth}

367   transports for April-March. (c) Seasonal cycle of C_{anth} transports using monthly data and 3 month

368   low-pass filtered data, error envelope of 1 s.d. (d) Ten-day and three month low-pass (bold) time

369   series of total anthropogenic carbon transport (black) and its overturning (blue) and horizontal

370   (orange) components. Dashed lines indicate the linear trend over the same timeframe. Positive

371   values indicate northward transport.

372

373
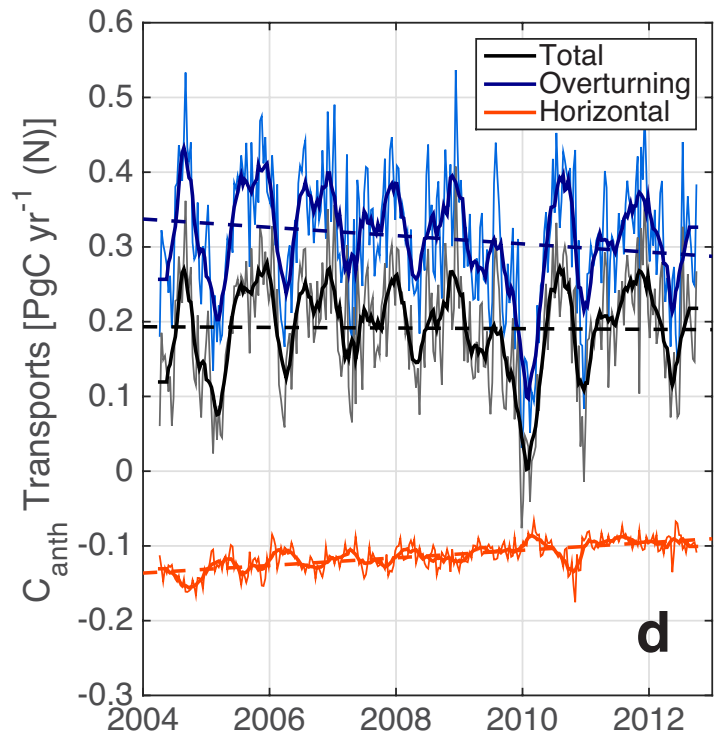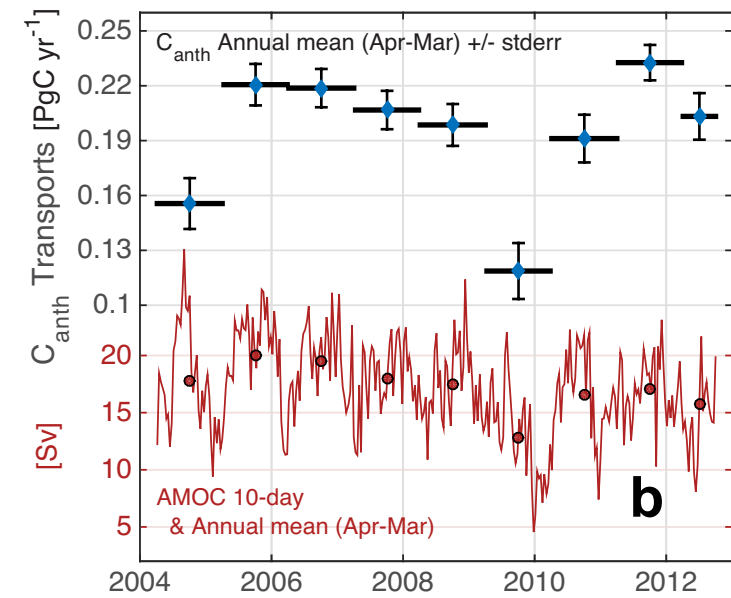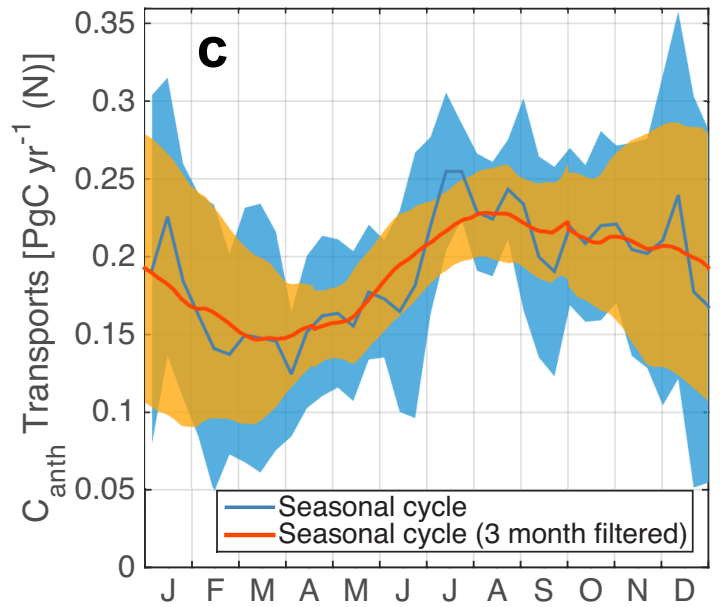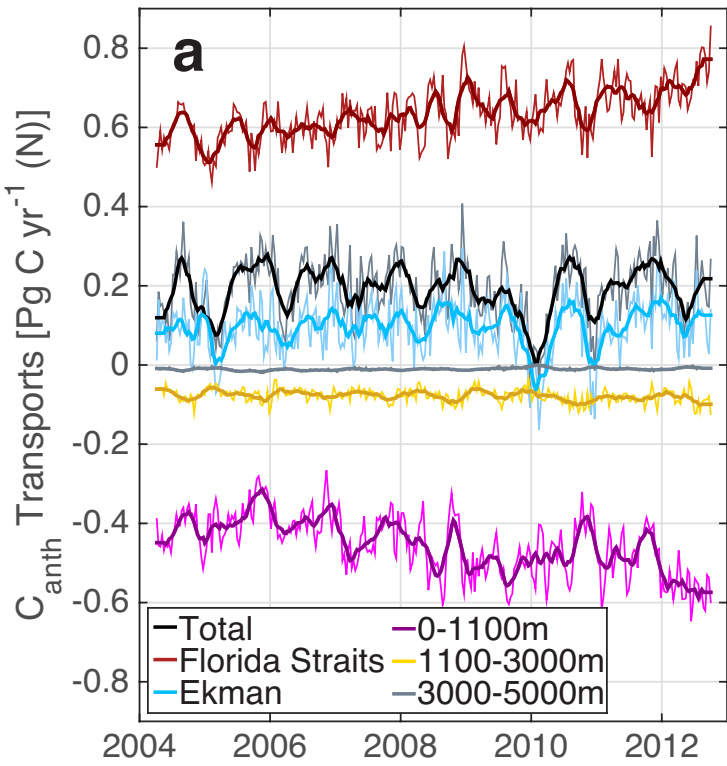
374   Figure 3. AMOC-C_{anth} transport co-variability and non-AMOC variability.

375   (a) The relationship between strength of meridional overturning circulation and magnitude of

376   C_{anth} transport at 26.5°N. Colour scale relates each data point to the time series in Fig. 1.

377   Diamonds represent April to March annual means with AMOC values from ref 17. (b) Residual

378   between observed C_{anth} transport and that predicted by linear AMOC-C_{anth} transport relationship

379   versus time, describing variability that does not vary coherently with the AMOC. The dotted line

380   is the linear trend of this residual between April 2004 and October 2012.

381

382

a

C_{anth} flux = 0.0176*AMOC -0.112

b

C_{anth} flux residual: +0.0093*time -18.6099
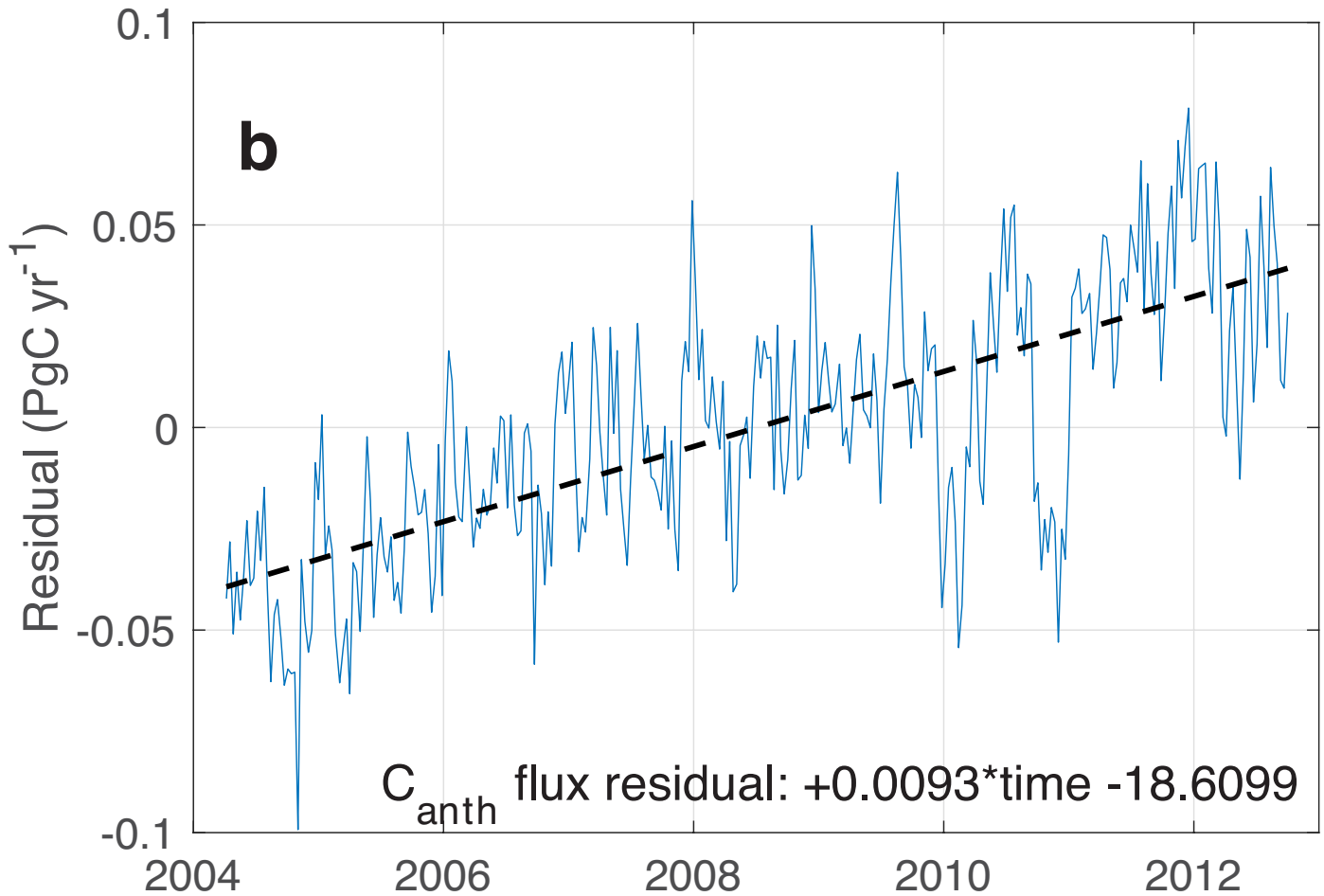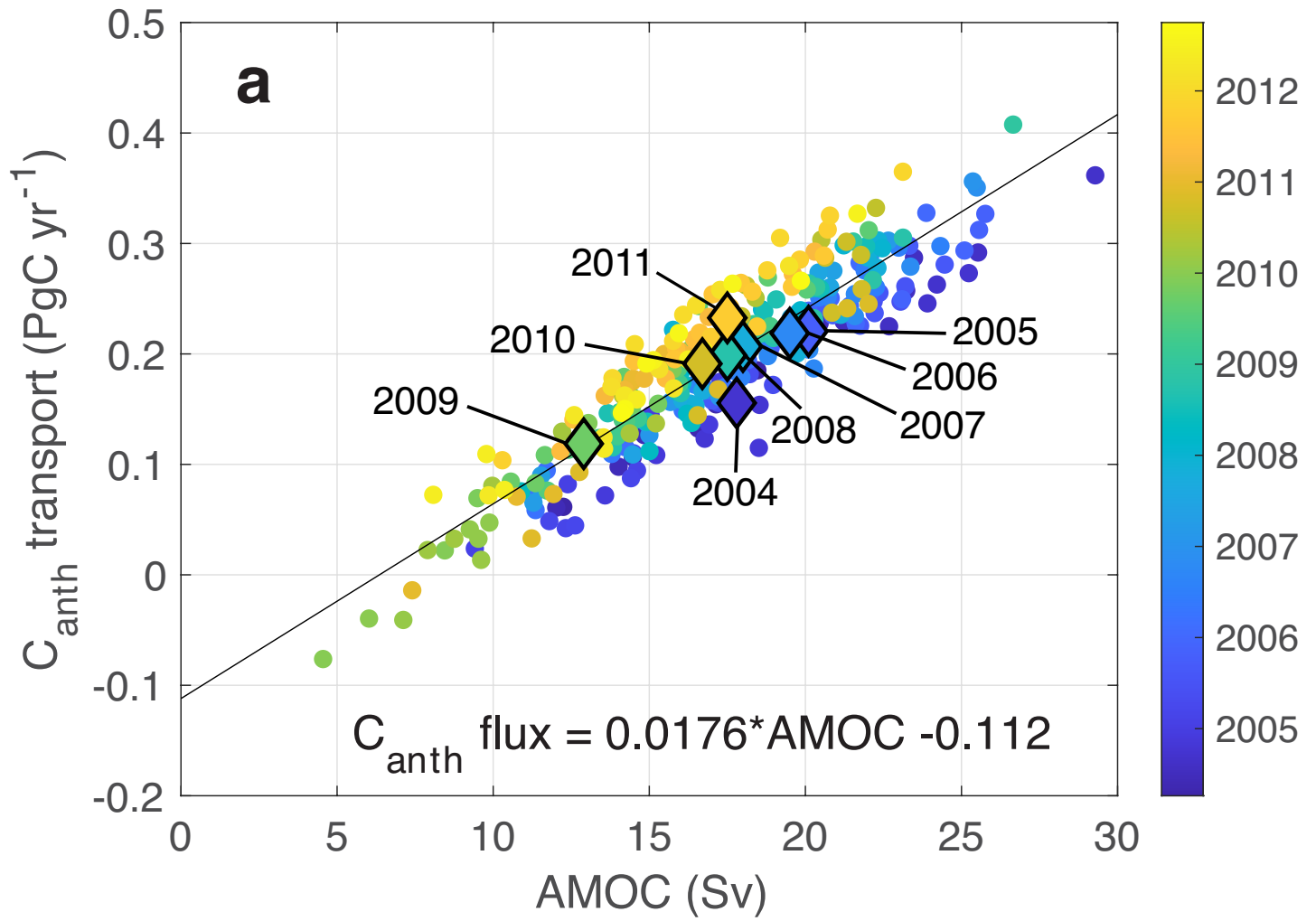
383   Figure 4. Impact of increasing anthropogenic carbon concentrations on ocean C_{anth} transport. (a)

384   Ten-day (normal) and three month low-pass (bold) time series of total C_{anth} transport including

385   (red) and ignoring (blue) effect of C_{anth} accumulating in the water column since 2002 for time-

386   period between April 2004 and October 2012. (b) Difference between the two time series in (a).

387   The effect of C_{anth} accumulating in the water column since 2002 on ocean C_{anth} transports at

388   26.5°N on ten-day (blue) and three month low-pass (black) time scales.

389

390

(a) Including water column C_{anth} increase

Excluding water column C_{anth} increase

(b) Contribution to transport of C_{anth} increasing in water column

10 day
3 months
Trend
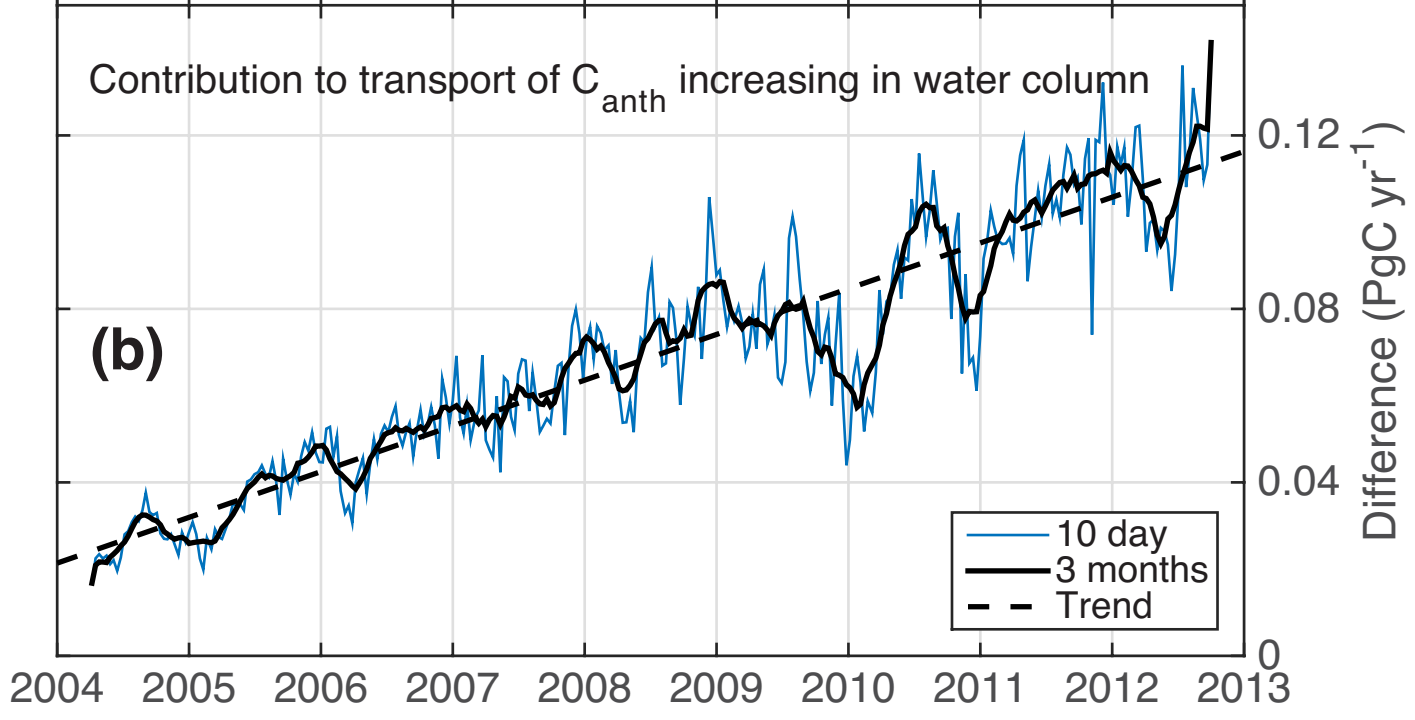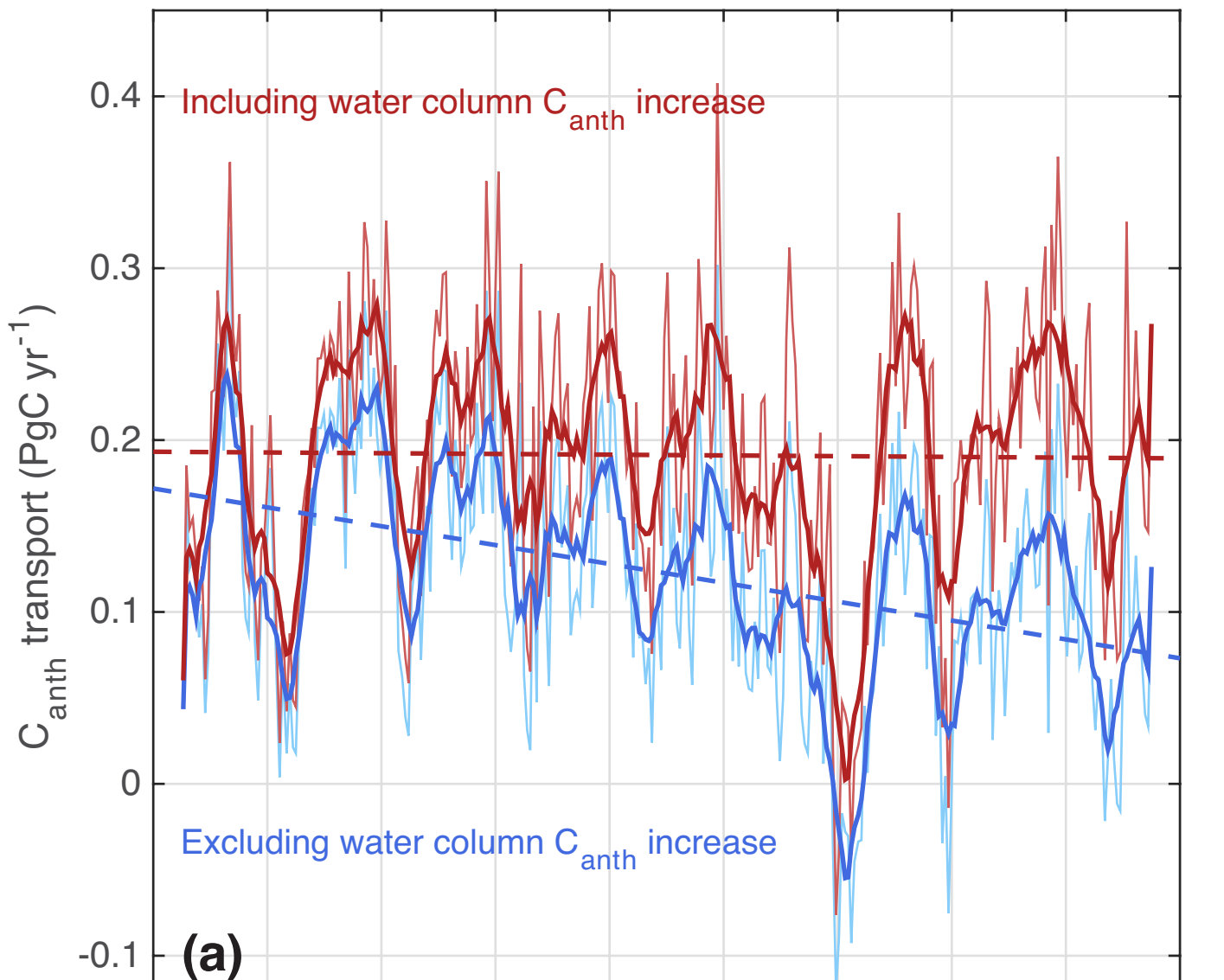
391

392

Method	Year	C_{anth} Transport (PgC yr^{-1}) & Contribution to storage[a]	Storage (PgC yr^{-1})	Air-sea C_{anth} flux (PgC yr^{-1}) & Contribution to storage	Citation
FROM GLOBAL ESTIMATES					
Biogeochemical Model	2000	0.15 ± 0.01	-	-	[20]
	2007	0.09 ± 0.02 (31%)	0.29	0.20 (69%)	[19]
Ocean Inversion	1995	0.12 ± 0.01 (33%)	0.39	0.28 (67%)	[18]
Ocean assimilation	2004	0.12 ± 0.01 (27%)	0.47	0.35 (73%)	[10]
Observational Integration	2000	-	0.38	-	[4]
FROM SYNOPTIC OBSERVATIONS					
Hydrographic sections	1992	0.24 ± 0.08 (58%)	0.43	0.18 (42%)	[16]
	1992	0.23 ± 0.08 (122%)	0.19-0.43[b]	-0.05 to 0.19 (-26 to 44%)	[14]
	1992	0.17 ± 0.06 (82%)	0.22[c]	0.04 (18%)	[13]
	1992	0.20 ± 0.02			[17]
	1998	0.20 ± 0.08 (95%)	0.22[c]	0.01 (5%)	[13]
	2004	0.25 ± 0.05 (66%)	0.39	0.13 (24%)	[15]
	2011	0.25 ± 0.02			[17]
This study	2004 to 2012	0.191 ± 0.013 47% to 41 %	0.39-0.47[d] to 0.45-0.53[d]	0.19-0.27 (~53%) to 0.25-0.33 (~59%)	
	2004	*0.16 ± 0.08 (36%)[e]*	*0.430[d]*		
	2005	*0.22 ± 0.07 (50%)[e]*	*0.438[d]*		
	2006	*0.22 ± 0.06 (49%)[e]*	*0.445[d]*		
	2007	*0.21 ± 0.06 (46%)[e]*	*0.453[d]*		
	2008	*0.20 ± 0.07 (43%)[e]*	*0.460[d]*		
	2009	*0.12 ± 0.09 (25%)[e]*	*0.468[d]*		
	2010	*0.19 ± 0.08 (40%)[e]*	*0.475[d]*		
	2011	*0.23 ± 0.06 (48%)[e]*	*0.483[d]*		
	2012	*0.20 ± 0.08 (41%)[e]*	*0.490[d]*		

393

21

394   Table 1. Summary of historical estimates of C_{anth} transport across 26.5°N, and storage / air-sea

395   flux terms derived from North Atlantic C_{anth} budgets. [a]Relative contribution to storage reflects

396   total oceanic C_{anth} transport and thus includes Bering Strait contribution. [b]Storage range

397   calculated following ref [14], using range of surface layer carbon change of 0.75-1.75 µmol kg^{-1}.

398   [c]Storage term calculated as residual of other components (transport, air-sea fluxes). [d]Storage

399   estimates for 2004 (and scaled to 2012) from refs [10] and [18]. [e]Annual averages are calculated on an

400   April to March basis due to time series beginning in April 2004; contributions to storage are

401   calculated as an average from different storage estimates.

402

403

Variable	Volume transport		Transport-weighted C_{anth}		C_{anth} transport		Contribution to C_{anth} transport trend due to	
	Mean (s.d.)	Trend (standard error)	Mean (s.d.)	Trend (standard error)	Mean (s.d.)	Trend (standard error)	Volume transport changes	C_{anth} field changes
	Sv	Sv yr^{-1}	µmol kg^{-1}	µmol kg^{-1} yr^{-1}	TgC yr^{-1}	TgC yr^{-2}	TgC yr^{-2}	TgC yr^{-2}
Florida Straits	31.58 (2.71)	-0.091 (0.062)	54.4 (3.9)	1.57 (0.0001)	634 (68)	17 (1.3)	-2	19
Ekman	3.53 (2.56)	0.002 (0.059)	74 (9.2)	1.19 (0.2)	97 (71)	2 (2)	0.1	2
Interior: Waters between 0 and 1,100 db minus Ekman	-18.37 (3.43)	-0.476 (0.074)	65.6 (4.4)	0.86 (0.09)	-453 (76)	-18 (1.5)	-12	-6
Waters between 1,100 and 3,000 db	-12.25 (2.26)	0.004 (0.052)	16.7 (1.52)	0.38 (0.03)	-77 (17)	-2 (0.4)	0	-2
Waters between 3,000 and 5,000 db	-6.45 (2.82)	0.477 (0.059)	4.4 (1.18)	0.11 (0.03)	-10 (4)	0.6 (0.1)	0.8	-0.3
Total					191 (79)	-0.4 (2)	-11	11
Horizontal	0 (0)	0 (0)			-114 (20)	5 (0.4)	0	5
Overturning	17.21 (4.13)	-0.55 (0.09)			312 (88)	-6 (2)	-10	4

Section average C_{anth} concentration: 14.7 µmol kg^{-1} in 2004 to 17.1 µmol kg^{-1} in 2012

404

405   Table 2. Averages and trends for different components of C_{anth} transports, volume transports, and

406   transport-weighted anthropogenic carbon concentrations with associated standard deviation /

407   standard error estimates, and their contribution to C_{anth} transport trends.

408   Transport-weighted C_{anth} concentrations are calculated by dividing the C_{anth} transport by the

409   volume transport. Volume transport values come from ref [23]. The interior relates to the ocean

410   east of the Bahamas (essentially all transport excluding Florida Straits). 1000 TgC = 1 PgC.

411

412

413   METHODS

414   **Hydrographic Data**. Dissolved inorganic carbon (DIC), total alkalinity, oxygen, dissolved

415   inorganic nutrients [nitrate, phosphate, silicate], CFC-12 and salinity from bottle samples

416   combined with temperature and pressure data from CTD sensors were used from repeat cruises at

417   24.5°N in 1992[14,36], 1998[13], 2004[37], 2010[38] and 2011[39] and across the Florida Straits in 2012[40].

418   Data consistency was ensured by comparing with historical data as part of GLODAPv2.2019[41];

419   all adjustments identified were applied. C_{anth} was calculated for each bottle using four techniques

420   (φCT_o[42], TrOCA[43], ΔC^*[44], Transit Time Distributions-TTD[45]) following established methods[39].

421   Although its representativeness is questioned[46] TrOCA was included to enable comparison with

422   previous studies[9,39,42].

423

424   Mixed layer bottle locations (density within $\sigma\theta = 0.03$ kg m^{-3} of the surface[47]) were treated

425   separately as here traditional techniques struggle to quantify C_{anth} and its seasonal cycle - either

426   relationships between nutrient utilisation, remineralisation and oxygen concentrations (used

427   within back-calculation methods) break down, or the behaviour of CFCs and CO_2 (used by TTD

428   and ΔC^* methods) decouple[48] due to their saturation state being dependent on distinct processes

429   (for example, temperature (both), biology and Rf (carbon only)). Mixed layer C_{anth} was therefore

430   calculated using a new method: SPIDEr (Scaled Pre-industrial DisEquilibrium).

431

432   **SPIDEr method for mixed layer anthropogenic carbon**. This circumvents/corrects a number

433   of assumptions inherent in many C_{anth} methods (for example, constant pre-industrial seasonal

434   atmospheric CO_2 concentration, CO_2 disequilibrium unchanged from pre-industrial era, oxygen

435   at 100% saturation). Extended Data Figure 4 summarizes the calculation pathway applied to

436   individual 4°latitude x 5° longitude boxes between 24-28°N and 78-12°W, and an additional

437   Florida Straits box (25-27°N, 80.2-79.3°W). It involves the following:

438   1. Calculate regional seasonal cycles in sea surface pCO_2 disequilibrium from modern

439   observations: following ref [49], historical observations of contemporary sea surface fCO_2 are from

440   the Surface Ocean Carbon Dioxide Atlas (SOCAT) database[50] and temporally coincident

441   observations of the dry mole fraction of atmospheric CO_2 (XCO2) are from ref. [51]; both were

442   converted to pCO_2[52] using in situ temperature and NCEP local sea-level atmospheric pressure

443   fields[53] to generate regionally-specific ΔpCO_2 time series. Mean annual ΔpCO_2 cycles were

444   calculated by Fourier analysis; their removal from the sea surface timeseries revealed no

445   significant trend between 2002-2012; the mean ΔpCO_2 cycle (winter-spring undersaturation,

446   summer-fall oversaturation) was therefore considered representative of the observational period.

447   2. Adjust seasonal ΔpCO_2 cycles to pre-industrial era by estimating the difference between the

448   impact of physical (temperature/salinity) and biological (nutrient) changes on modern and pre-

449   industrial carbon concentrations. Spring-to-fall changes in temperature/salinity were calculated

450   from climatological data[54] and applied to annual mean climatological chemical properties (DIC,

451   alkalinity, salinity, nutrients[54]) using CO2SYS[55] to propagate their impact on ΔpCO_2. The impact

452   of biological activity was estimated using winter-to-summer changes in phosphate converted to

453   ΔDIC using a C/P stoichiometric ratio of 117 following the 'ΔC^*' C_{anth} method – this integrative

454   C/P estimate has been successfully applied in the Atlantic and globally to derive C_{anth} fields and

455   enhance intercomparison of studies[4,29,56], but likely underestimates true system variability[57];

456   ΔDIC was then applied to annual mean climatological chemical properties (temperature,

457   alkalinity, salinity[54]) using CO2SYS[55] to calculate biologically-mediated ΔpCO_2. Both steps

458   were repeated for a pre-industrial scenario by removing the mean annual C_{anth} signal (calculated

459   using the φCT_o method applied to climatological data) from contemporary DIC levels; changes

460   in pre-industrial pCO_2 caused by temperature or biological activity were 69-72% of the change in

461   pCO_2 observed at contemporary DIC levels.

462   3. Combine pre-industrial ΔpCO_2 seasonal cycles with estimated pre-industrial atmospheric CO_2

463   seasonal cycles to generate 4°latitude x 5° longitude box-specific pre-industrial seawater pCO_2

464   cycles. Pre-industrial atmospheric CO_2 is calculated from modern GLOBALVIEW-CO2

465   atmospheric CO_2[51] combined with NCEP/NCAR temperature and sea level pressure fields[53] and

466   deconvolved into a long-term atmospheric C_{anth} increase and a seasonally variable natural

467   background signal.

468   4. Using in situ alkalinity and nutrients (assumed unaffected by anthropogenic CO_2 invasion)

469   with pre-industrial pCO_2 at the time of year of the modern measurements, calculate the water

470   sample's pre-industrial DIC.

471   5. The residual between pre-industrial and contemporary DIC concentrations is C_{anth}.

472

473   **RAPID-MOCHA-WBTS-Argo array data**. Ten-day temperature and salinity fields across

474   26.5°N[26] were used to calculate volume transports and ten-day C_{anth} fields. For the upper 1,760

475   dbar, 0.25° longitude × 20 dbar grids of temperature and salinity are generated every 10 days by

476   optimal interpolation of data from Argo floats and moored sensors; below 1,760 dbar, salinity

477   and temperature fields are linearly interpolated between moored sensors on the boundaries, with

478   regions deeper than the moorings accounted for by extrapolation based on repeat hydrography

479   abyssal structure. Volume transports were calculated by combining horizontal velocities from the

480   gridded fields with circulation elements in the RAPID overturning calculation[21]. The UK-US

481   RAPID array (Fig. 1) uses submarine-cable-based transport estimates through the Florida Straits

482 at 27°N[58], ERA-Interim wind derived estimates of Ekman transport[59] and ocean interior transport

483 estimates from moored data. The calculations generate a net volume (or freshwater) transport of

484 1.17 Sv southward across 26.5°N on the basis of a salinity flux constraint at the Bering Strait [26].

485

486 **Predictive regression equations (PREs) for C_{anth}.**

487 For each C_{anth} method, C_{anth} is determined for all available hydrographic bottle data prior to

488 recalculating mixed layer values according to the SPIDEr approach. Linear C_{anth} growth rates

489 were calculated in six isopycnal intervals (uNACW: $\sigma_0 < 26.7$ kg m^{-3}, lNACW: 26.7 kg m^{-3}

490 $< \sigma_0 < 27.2$ kg m^{-3}, AAIW: 27.2 kg m$^{-3} < \sigma_0 < 27.6$ kg m^{-3}, uNADW: $\sigma_0 > 27.6$ kg m^{-3} and $\sigma_2 < 37$ kg

491 m^{-3}, lNADW: $\sigma_2 > 37$ kg m^{-3} and $\sigma_4 < 45.9$ kg m^{-3}, AABW: $\sigma_4 > 45.9$ kg m^{-3}) in five longitude

492 ranges (Florida Straits, 78-70°W, 70-46°W, 46-30°W, 30-10°W)[39], and used to normalise all

493 C_{anth} data to a mid-year of 2002.5. As the constituent data are from multiple seasons, the pooled

494 normalised data cover a greater parameter range than individual hydrographic cruises,

495 particularly in surface waters. Predictive regression equations (PREs) are generated by applying

496 multiple linear regressions of the normalised C_{anth} according to $normC_{anth} = a*\theta + b*Sal + c*pres$

497 $+ d*lon + y^0$, where a-d are predictive coefficients, 'θ' is potential temperature, 'Sal' is salinity,

498 'pres' is pressure, 'lon' is longitude and 'y^0' is a constant. Individual PREs are generated for

499 each isopycnal-regional box as in Extended Data Fig. 1, with outliers identified using a 3x mean

500 Cook's Distance discriminating threshold and removed prior to rerunning. Extended Data Table

501 1 shows PRE coefficients for the ΔC^* C_{anth} method. PRE root-mean-square errors (Extended

502 Data Fig. 1b) are largest (but lowest relative to signal size) in surface layers where C_{anth} loadings

503 and seasonal variability are highest, but are generally at or below C_{anth} estimation uncertainty (~6

504 μmol kg^{-1}). PRE goodness-of-fit (Extended Data Fig. 1c) shows greater variability, and

505 highlights where either the predictive parameter is insufficiently covered by available

506 measurements, or where the predictive parameters do not co-vary sufficiently with C_{anth}. PREs

507 perform less well where C_{anth} levels change quickly with depth but temperature and salinity do

508 not (typically ~800-1800 dbar, associated with C_{anth} minimum and maximum of Antarctic

509 Intermediate Water and upper North Atlantic Deep Water respectively). PRE residuals are

510 normally distributed about zero with no apparent vertical or spatial structure (Extended Data Fig.

511 2). However, PRE goodness-of-fit plots (Extended Data Fig. 3) display a general trend of

512 regressions over(under)-estimating lower (higher) concentrations; that is estimated values tend

513 towards the isopycnic/regional box mean. The variability in available predictive parameter space

514 (temperature, salinity, pressure, longitude) thus does not fully describe C_{anth} variability, but on a

515 regional box basis uncertainties will likely cancel and errors in predicted values tend towards the

516 regional C_{anth} mean. For all methods, analyses of standardized (Z-score) predictors identify

517 salinity as the most important predictor variable, except in the upper layers away from the

518 western boundary where temperature and pressure have similar influence.

519

520 **Ten-day estimates of C_{anth}.** For each ten-day period between spring 2004 and fall 2012, the

521 predictive regressions are applied to temperature and salinity fields[26] derived from RAPID

522 mooring / Argo float data (binned according to Extended Data Fig. 1a criteria) to estimate C_{anth}.

523 The mixed layer is defined as the maximum mixed layer depth (MLD, determined using density

524 within $\sigma\theta = 0.03$ kg m^{-3} of the surface[47]) from the preceding winter – ensuring that winter waters

525 temporarily isolated from atmospheric interaction during summer are still described by the same

526 regression equation as the waters above, rather than falling within the bin below. Predicted

527 surface layer C_{anth} (Extended Data Fig. 5 for 2009, 63.375°W) shows highest concentrations (late

528 summer/early fall) associated with potential temperature maxima and neutral density, Rf and

529 MLD minima. The C_{anth} signal is diluted as cooling drives stratification breakdown, reaching a

530 spring minimum as MLD (and Rf) peaks. Pooled together, ten-day estimates of time-independent

531 C_{anth} (normalized to 2002.5) are created. For each time-point ΔC_{anth} growth rates are

532 reintroduced, using identical linear trends that normalized the original data set, generating final

533 C_{anth} estimates reflective of the 2004-2012 time period.

534

535 **C_{anth} transports across 26.5°N**. Ten-day C_{anth} and velocity fields are combined according to

536 $T_{(Canth)}=\iint \upsilon C_{anth}\, dxdz$, where the C_{anth} transport, $T_{(Canth)}$, is given by the horizontal (x) and vertical

537 (z) integral of the C_{anth} field multiplied by the velocity field υ[17]. The overturning transport

538 component $T^{o}_{(Canth)}$ is calculated as $T^{o}_{(Canth)}=\int \langle \upsilon \rangle \langle C_{anth} \rangle dz$, where zonally-averaged fields of

539 anthropogenic carbon $\langle C_{anth} \rangle$ and velocity $\langle \upsilon \rangle$ with section average removed are combined and

540 vertically integrated (z) across the full section. The horizontal transport component $T^{h}_{(Canth)}$

541 meanwhile is calculated as $T^{h}_{(Canth)}=\iint \upsilon'\, C_{anth}'dxdz$, and is the horizontal (x) and vertical (z)

542 integral of the combination of the deviation from the zonal-mean anthropogenic carbon C_{anth}' and

543 velocity υ' fields. The throughflow component $T^{tf}_{(Canth)}$ is calculated as $T^{tf}_{(Canth)} = T^{tf}(C_{anth}'^{(26.5N)}$ -

544 $C_{anth}'^{(BS)})$ where C_{anth}' is the zonal-mean field for C_{anth} at 26.5°N (calculated here) and Bering

545 Strait (BS, from ref [15]) and T^{tf} is the net volume throughflow transport. The Florida Straits are

546 treated separately; here, C_{anth} (including updated mixed layer C_{anth} estimates) from hydrographic

547 sections in 2004, 2010 and 2012 (US GOMECC[40]) are combined with volume transport

548 estimates derived from hydrographic CTD profiles. Transport-weighted C_{anth} estimates are used

549 to create temporally predictive regressions (Extended Data Fig. 6a) that are applied to the high-

550 frequency time series of subsea-cable-derived volume-transport estimates. Combining Florida

551   Straits C_{anth} transports with ocean interior analogues yields ten-day C_{anth} transports across 26.5°N

552   (Extended Data Fig. 6b,c). All C_{anth} methods show small, temporally consistent systematic

553   offsets from each other. These are due to slight differences in mean surface-to-depth C_{anth}

554   gradients caused by the differing methodological assumptions of each technique. The TTD

555   method is an exception; its offset changes with time, resulting from using CFC-12 alone to

556   estimate mean water mass age. Decreasing atmospheric CFC-12 levels since ~2000 inhibit its

557   ability to fully characterise the ventilation of the youngest waters, but it is the only transient

558   tracer to have been measured on all hydrographic cruises with carbon data.

559

560   **Uncertainties in C_{anth} transport estimates from observations**. Following the approach used

561   for salinity and freshwater transports across 26.5°N[26] the uncertainty of individual ten-day

562   normalized C_{anth} transport estimates is calculated by estimating and combining C_{anth}-derived

563   uncertainty (σCT_C) and transport-derived uncertainty (σCT_T). The uncertainty associated with

564   both initial estimates of C_{anth} and the linear trends in C_{anth} (treated independently in the full

565   section and Florida Straits) is then also assessed. The two combine to generate final C_{anth}

566   transport uncertainties. For each subregion, σCT_C is calculated by combining the uncertainty in

567   C_{anth} concentrations (σC_{reg}) with the average volume transport (T_{reg}). The transport-derived

568   uncertainty is calculated by combining the subregional transport uncertainty σCT_T and the C_{anth}

569   anomaly ($C_{reg} - C_{sect}$) where the C_{anth} section average is 19.2 µmol kg^{-1}. Uncertainties were

570   calculated for individual regional water masses, the Bering Strait, the Ekman layer, and the

571   Florida Straits[26] (Extended Data Table 2). Uncertainty relating to input C_{anth} fields and ΔC_{anth}

572   trends was calculated by a Monte-Carlo approach: individual systematic offsets randomly

573   derived from a normal distribution of twice the estimation uncertainty (6 µmol kg^{-1}) were applied

574   to each input hydrographic cruise dataset while similar offsets were applied to trends, randomly-

575   derived from within the trend uncertainties[39]. The average standard deviation of 600 individual

576   estimates at each timepoint gave an uncertainty of 0.037 PgC yr^{-1}. Combining all the above

577   uncertainties in quadrature generates an estimate of the total uncertainty for each ten-day C_{anth}

578   transport estimate of 0.135 PgC yr^{-1}. If it is assumed that within a year there can be 12

579   independent estimates of the C_{anth} transport, then uncertainty in the annual average C_{anth} transport

580   is $0.135 / (12)^{1/2} = 0.039$ PgC yr^{-1}. For the 8.5-year time series there are then 102 independent

581   estimates of the C_{anth} transport, meaning the uncertainty of the full time series average C_{anth}

582   transport is $0.135 / (102)^{1/2} = 0.0134$ PgC yr^{-1}.

583

584   **Uncertainties from surface C_{anth} seasonality calculation**

585   The impact of not accounting for seasonality in surface C_{anth} concentrations was investigated by

586   propagating three additional surface C_{anth} estimates to that described in the preceding section

587   through the C_{anth} transport calculation: (1) using unadjusted raw bottle C_{anth} estimates; (2)

588   assuming C_{anth} to be 100% saturated at all times; (3) applying SPIDEr (Extended Data Figure 4),

589   but assuming modern and pre-industrial ΔpCO_2 cycles are identical. For (1) the C_{anth} seasonal

590   cycle amplitude was ~3x larger than any other application (and implausible through what we

591   know of sea-surface CO_2 flux dynamics); much higher C_{anth} concentrations for ~9-10 months of

592   the year, resulted in elevated Ekman, horizontal and total C_{anth} transports (with full time series

593   average ~15% higher) and exaggerated seasonal cycles in each. A negligible horizontal transport

594   trend led to the total C_{anth} transport trend becoming negative. For cases (2) and (3), a reversed

595   seasonal cycle resulted: C_{anth} highest (lowest) in winter (summer), the opposite to that expected

596   from Rf variability[5,54]. In (2), a greatly reduced west-to-east gradient in C_{anth} concentrations

597   resulted, leading to reduced southward horizontal circulation and a total transport average ~12%

598   higher than that presented here. In (3), a west-to-east concentration gradient was maintained but

599   at systematically higher concentrations; this generated stronger C_{anth} overturning and horizontal

600   components but to differing extents, causing a net decrease in the average total C_{anth} transport of

601   ~4% compared to results presented here. Failing to account for seasonality in CO_2 disequilibria

602   and C_{anth} can therefore generate inverted seasonal cycles, and unfeasible concentration ranges

603   and longitudinal gradients. These subsequently affect calculated Ekman, horizontal, overturning

604   and total C_{anth} transports and their trends, and may be a factor in previous hydrographic section-

605   derived C_{anth} transport estimates.

606   **Uncertainties in C_{anth} transport estimates from PRE and C_{anth} methodologies**. We test the

607   robustness and appropriateness of the PRE method using an analysis of model data where model

608   C_{anth} truth is known. We use monthly fields from the 1° NEMOv3.2 ocean model with the

609   MEDUSA-2 marine biogeochemistry model embedded (for example, ref. 60), between 1980 and

610   2100 across 26.5°N. Model truth C_{anth} was calculated as the residual of parallel runs (with

611   atmospheric growth of carbon and climate change effects at RCP8.5, and without), and combined

612   with directly output velocity fields to give C_{anth} transports for 2004-2013 of 0.223 ± 0.061 PgC

613   yr^{-1} (mean ± standard deviation of monthly values). PRE-predicted C_{anth} fields (estimated using

614   PRE methodology applied to model truth C_{anth}, temperature, pressure, salinity outputs as for

615   observations) were combined with the same velocity fields, enabling direct comparison with

616   model truth C_{anth} transports (Extended Data Fig. 7). Within this, several experiments were

617   conducted, adjusting PRE data and trend inputs/treatments additively, to quantify the

618   contributions of individual PRE methodological assumptions and their impact on the overall

619   uncertainty in C_{anth} transport estimates. These were: (1) PRE method applied as for observations,

620   using same vertical data resolution (~20 data points per station), input data timepoints (one

621   month each from 1992-1998-2004-2010-2011), identical longitudinal/isopycnal boxes optimised

622   to observational hydrographic distributions, and assuming linear ΔC_{anth} trends; (2) PRE regions

623   optimised to model hydrographic distributions/transport fields (these differed substantially from

624   observations due to low model resolution); (3) PRE training data extended to cover all months of

625   years 1992-1998-2004-2010-2011; (4) non-linear ΔC_{anth} trends; and (5) increased vertical data

626   resolution (~60 data points per station). Iteration (1) resulted in a 2004-2013 C_{anth} transport mean

627   ± standard deviation of 0.234 ± 0.059 PgC yr^{-1}, a net residual from the model truth of 5% (0.011

628   PgC yr^{-1}), with essentially identical monthly variability. Approximately 35% of the residual from

629   model truth was explicable by insufficient vertical data resolution, ~23% by the assumption of

630   linear C_{anth} growth rates, and the remainder due to PRE regions being poorly optimised to local

631   hydrographic/transport fields. Iteration (2) was most faithful to the method's application to

632   observations, and gave a 2004-2013 mean ± standard deviation of 0.229 ± 0.061 PgC yr^{-1}, a

633   2.9% residual from model truth (0.223 ± 0.061 PgC yr^{-1}). Individual monthly transport estimates

634   had an average absolute residual of 4%, with best estimates in May-June (average 1.6%

635   difference), poorest in September-October (average ~8.5% difference). Iteration (5) is considered

636   the best estimate of the abilities of the PRE method; for 2004-2013 it reduced the mean to within

637   1% of model truth, and average absolute residuals of monthly estimates to 2.5%. This underlines

638   the suitability of the PRE methodology in estimating the magnitude of C_{anth} transports over

639   multiple timescales, and application to observational datasets.

640   'Back-calculation' C_{anth} estimation methods have been widely used to quantify the accumulation

641   of C_{anth} in the oceans[e.g.4,5,9,13–15,17,37,39,42–44,56,61,62], and we applied three derivations based on

642   biogeochemical parameters to observations. Of these we applied the ΔC^* method[44] to model

643   outputs to test its effectiveness in estimating C_{anth} distributions and C_{anth} transport variability and

644   magnitude compared to model truth. Ref [44] was followed for the calculation of 'ΔC^*', but using

645   alternative parameterizations for preformed alkalinity[63] and preformed pre-industrial DIC[62]. The

646   disequilibrium term was determined from 'ΔC^*' derived from the model control run (with a pre-

647   industrial atmosphere). C_{anth} estimates were combined with model velocity fields and the

648   resultant C_{anth} transports compared to model truth (Extended Data Fig. 8). A correlation of 0.97

649   between the two time series occurred with an average residual of 2.2 x10^{-4} PgC yr^{-1} (0.5%) for

650   the 2004-2013 period. Individual monthly transport estimates had mean absolute residuals of

651   7.2%, and annual average absolute differences of 0.010 PgC yr^{-1} (4.5%). These differences are

652   small, predominantly caused by control run 'ΔC^*' drift and deficiencies in the model's

653   biogeochemical fields that impact the use of observation-based parameterizations (for example

654   preformed alkalinity). Together, the estimates indicate that the back-calculation is useful for

655   estimating C_{anth}.

656

657

658   DATA SOURCES

659   Raw hydrographic datasets are at https://cchdo.ucsd.edu/. Final adjusted hydrographic datasets

660   are available from GLODAP (https://www.glodap.info/). AMOC estimates are available from

661   the RAPID programme website (https://www.rapid.ac.uk/).

662   Atmospheric CO_2 is available from the GLOBALVIEW-CO2 web resources (GLOBALVIEW-

663   CO2. Cooperative Atmospheric Data Integration Project - Carbon Dioxide; NOAA ESRL,

664   Boulder, Colorado; Also available on Internet via anonymous FTP to ftp.cmdl.noaa.gov, Path:

665   ccg/co2/GLOBALVIEW). Sea surface pCO_2 observations are from the Surface Ocean Carbon

666   Dioxide Atlas SOCAT: https://www.socat.info/. NCEP/NCAR temperature and sea level

667   pressure fields are available from

668   https://psl.noaa.gov/data/gridded/data.ncep.reanalysis.surface.html.

669

670   DATA AVAILABILITY

671   The carbon transport data that support the findings of this study are available from the British

672   Oceanographic Data Centre (https://www.bodc.ac.uk/) at

673   https://www.bodc.ac.uk/data/published_data_library/catalogue/10.5285/b6bb9f45-f562-68a4-

674   e053-6c86abc0e48b/. The doi of this dataset is 10.5285/b6bb9f45-f562-68a4-e053-

675   6c86abc0e48b, and the data citation is : Brown P.J., McDonagh E., Sanders R., Watson A.J.,

676   Wanninkhof R.H., King B.A., Smeed D., Baringer M.O., Meinen C.S., Schuster U., Yool A.,

677   Messias M. (2020). Anthropogenic carbon transports at 26N as estimated using the RAPID-

678   MOCHA-WBTS (RAPID-Meridional Overturning Circulation and Heatflux Array-Western

679   Boundary Time Series) array for 2004 to 2012. British Oceanographic Data Centre - Natural

680   Environment Research Council, UK. doi: 10/fn4j. The dataset will also be accessible from the

681   RAPID-Atlantic Biogeochemical Fluxes programme webpage (http://www.rapid.ac.uk/abc).

682

683

684

685   METHODS REFERENCES

686   36. Guallart, E. F., Pérez, F. F., Rosón, G. & Ríos, A. F. High spatial resolution Alkalinity and

687   pH measurements along 24 . 5 ° N in 1992 Institut de Ciències del Mar , CSIC Passeig

688   Marítim de la Barceloneta , 37-49 08003 Barcelona , Spain Instituto de Investigaciones

689   Marinas , CSIC Eduardo Cabello , 6 Facultad . 5, (2010).

690   37. Brown, P. J., Bakker, D. C. E., Schuster, U. & Watson, A. J. Anthropogenic carbon

691   accumulation in the subtropical North Atlantic. J. Geophys. Res. 115, C04016 (2010).

692   38. Schuster, U. et al. Measurements of total alkalinity and inorganic dissolved carbon in the

693   Atlantic Ocean and adjacent Southern Ocean between 2008 and 2010. Earth Syst. Sci. Data

694   6, 175–183 (2014).

695   39. Guallart, E. F. et al. Trends in anthropogenic CO2 in water masses of the Subtropical North

696   Atlantic Ocean. Prog. Oceanogr. 131, 21–32 (2015).

697   40. Wanninkhof, R. et al. Ocean acidification along the Gulf Coast and East Coast of the USA.

698   Cont. Shelf Res. 98, 54–71 (2015).

699   41. Olsen, A. et al. GLODAPv2.2019 – an update of GLODAPv2. Earth Syst. Sci. Data 11,

700   1437–1461 (2019).

701   42. Vázquez-Rodríguez, M. et al. Anthropogenic carbon distributions in the Atlantic Ocean:

702   data-based estimates from the Arctic to the Antarctic. Biogeosciences 6, 439–451 (2009).

703   43. Touratier, F., Azouzi, L. & Goyet, C. CFC-11, $\Delta14$ C and 3 H tracers as a means to assess

704   anthropogenic CO 2 concentrations in the ocean. Tellus B 59, 318–325 (2007).

705   44. Gruber, N., Sarmiento, J. L. & Stocker, T. F. An improved method for detecting

706   anthropogenic CO2 in the oceans. Global Biogeochem. Cycles 10, 809–837 (1996).

707   45. Waugh, D. W., Hall, T. M., Mcneil, B. I., Key, R. & Matear, R. J. Anthropogenic CO 2 in

708   the oceans estimated using transit time distributions. Tellus B Chem. Phys. Meteorol. 58,

709   376–389 (2006).

710   46. Yool, A., Oschlies, A., Nurser, A. & Gruber, N. A model-based assessment of the TrOCA

711   approach for estimating anthropogenic carbon in the ocean. Biogeosciences 7, 723–751

712   (2010).

713   47. de Boyer Montégut, C., Madec, G., Fischer, A., Lazar, A. & Iudicone, D. Mixed layer depth

714   over the global ocean: An examination of profile data and a profile-based climatology. J.

715   Geophys. Res. 109, C12003 (2004).

716   48. Álvarez, M. & Gourcuff, C. Uncoupled transport of chlorofluorocarbons and anthropogenic

717   carbon in the subpolar North Atlantic. Deep Sea Res. Part I Oceanogr. Res. Pap. 57, 860–

718   868 (2010).

719   49. Landschützer, P. et al. A neural network-based estimate of the seasonal to inter-annual

720   variability of the Atlantic Ocean carbon sink. Biogeosciences 10, 7793–7815 (2013).

721   50. Bakker, D. C. E. et al. A multi-decade record of high-quality fCO2 data in version 3 of the

722   Surface Ocean CO2 Atlas (SOCAT). Earth Syst. Sci. Data 8, 383–413 (2016).

723   51. GLOBALVIEW-CO2. Cooperative Atmospheric Data Integration Project - Carbon Dioxide;

724   NOAA ESRL, Boulder, Colorado; [Also available on Internet via anonymous FTP to

725   ftp.cmdl.noaa.gov, Path: ccg/co2/GLOBALVIEW]. (2011).

726   52. Körtzinger, A. Methods of Seawater Analysis, Chap. Determination of Carbon Dioxide

727   Partial Pressure (pCO2). Verlag Chemie 149–158 (1999).

728   53. Kalnay, E. et al. The NCEP/NCAR 40-Year Reanalysis Project. Bull. Am. Meteorol. Soc.
729   77, 437–471 (1996).

730   54. Takahashi, T. et al. Climatological distributions of pH, pCO2, total CO2, alkalinity, and
731   CaCO3 saturation in the global surface ocean, and temporal changes at selected locations.
732   Mar. Chem. 164, 95–125 (2014).

733   55. van Heuven, S., Pierrot, D., Rae, J. W. B., Lewis, E. & Wallace, D. W. R. MATLAB
734   Program Developed for CO2 System Calculations, ORNL/CDIAC-105b. (2011)
735   doi:10.3334/CDIAC/otg.CO2SYS_MATLAB_v1.1.

736   56. Gruber, N. Anthropogenic CO2 in the Atlantic Ocean. Global Biogeochem. Cycles 12, 165–
737   191 (1998).

738   57. Martiny, A. C. et al. Strong latitudinal patterns in the elemental ratios of marine plankton
739   and organic matter. Nat. Geosci. 6, 279–283 (2013).

740   58. Baringer, M. O. N. & Larsen, J. C. Sixteen years of Florida Current transport at 27 N.
741   Geophys. Res. Lett. 28, 3179–3182 (2001).

742   59. Dee, D. P. et al. The ERA-Interim reanalysis: configuration and performance of the data
743   assimilation system. Q. J. R. Meteorol. Soc. 137, 553–597 (2011).

744   60. Couldrey, M. P., Oliver, K. I. C., Yool, A., Halloran, P. R. & Achterberg, E. P. On which
745   timescales do gas transfer velocities control North Atlantic CO2 flux variability? Global
746   Biogeochem. Cycles 30, 787–802 (2016).

747   61. Álvarez, M., Ríos, A. F., Pérez, F. F., Bryden, H. L. & Rosón, G. Transports and budgets of
748   total inorganic carbon in the subpolar and temperate North Atlantic. Global Biogeochem.
749   Cycles 17, 1002 (2003).

750   62. Lee, K. et al. An updated anthropogenic CO2 inventory in the Atlantic Ocean. Global

751   Biogeochem. Cycles 17, art. no.-1116 (2003).

752   63. Brewer, P. G., Bradshaw, A. L., Shafer, D. K. & Williams, R. T. Measurements of total

753   carbon dioxide and alkalinity in the North Atlantic Ocean in 1981. in The Changing Carbon

754   Cycle: A Global Analysis (eds. Trabalka, J. R. & Reichle, D. E.) 348–370 (Springer, 1986).

755

756

757   EXTENDED DATA LEGENDS

758   **Extended Data Figure 1. PRE regions and performance statistics.** (a) Data bin locations for

759   generation of independent predictive multiple linear regressions for C_{anth} estimation, (b)

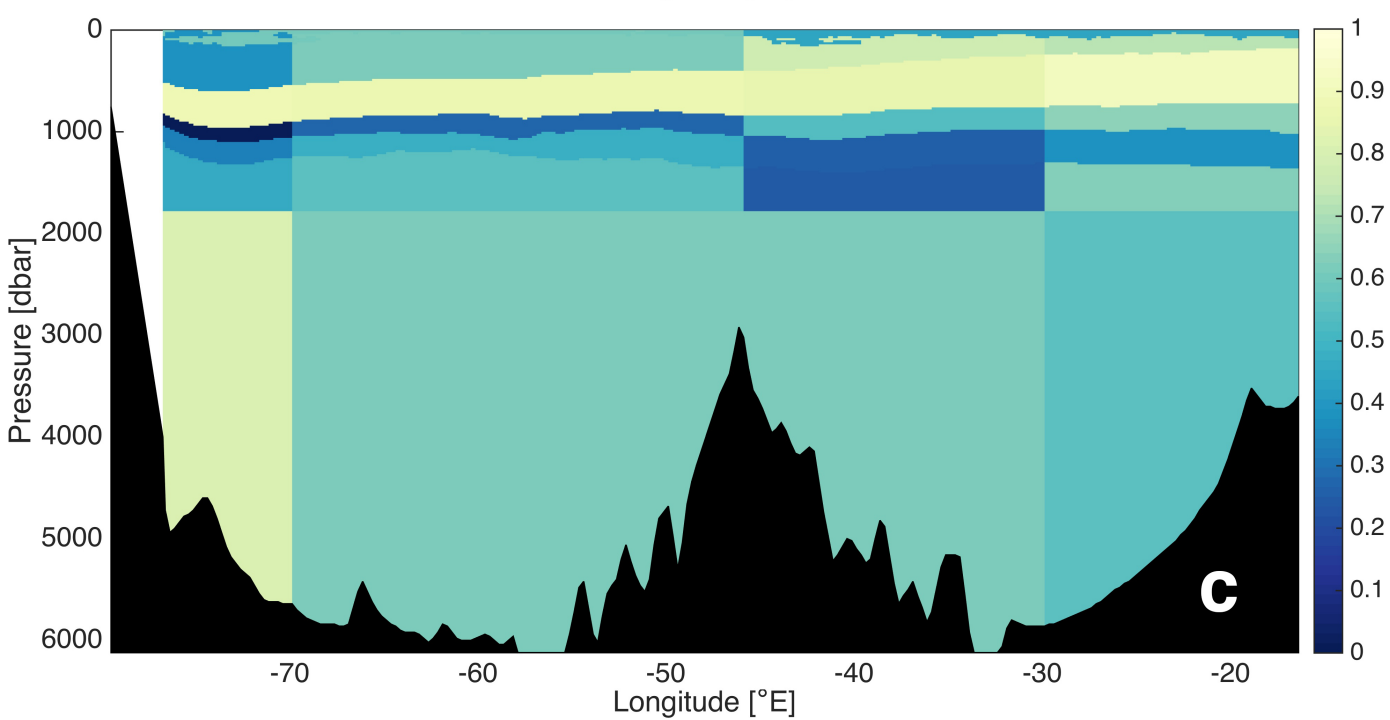760   individual predictive PRE root mean square error, and (c), individual predictive PRE R^2 for each

761   data bin for ΔC^* C_{anth}. Box colors and numbers relate to Extended Figures 3 & 4.

762

763
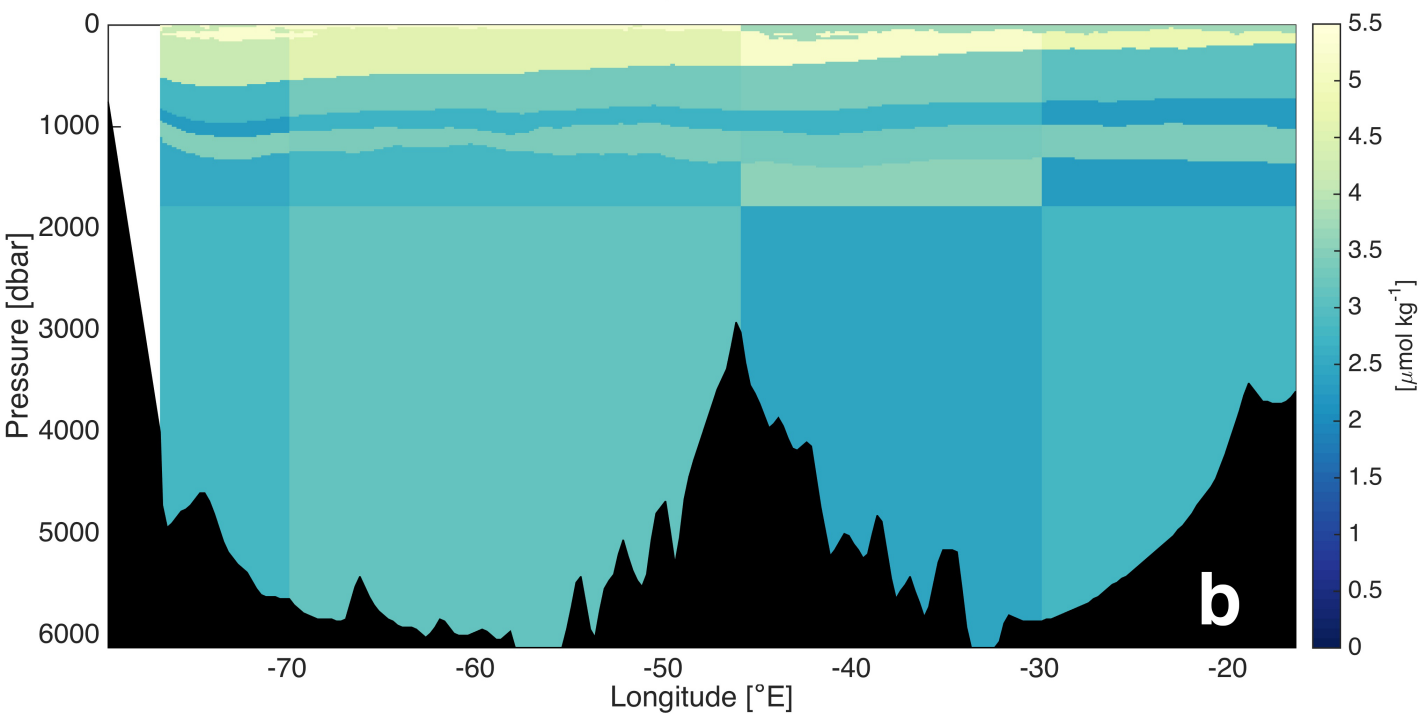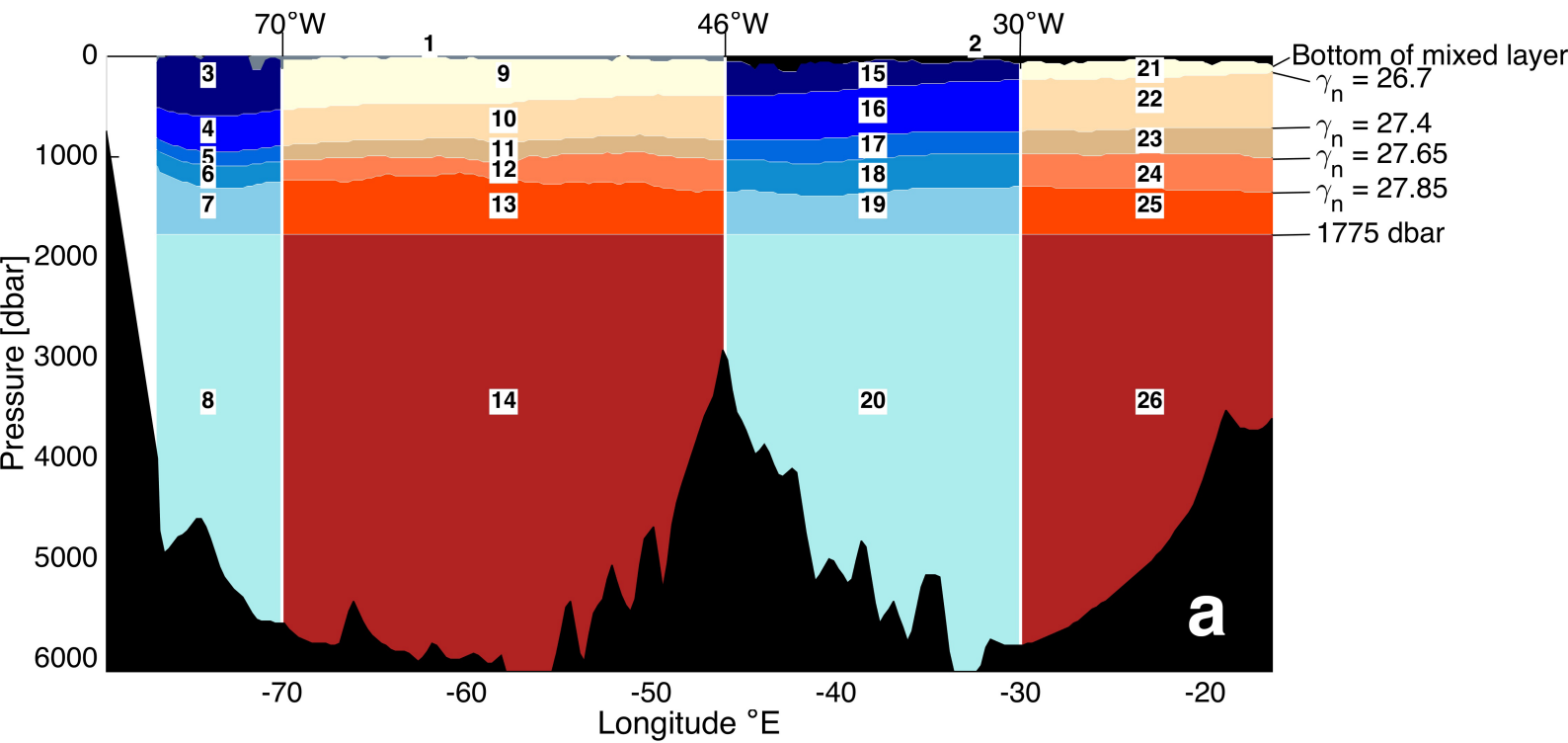
764   **Extended Data Figure 2. PRE residuals (predicted C_{anth} − bottle C_{anth}) plotted against**

765   **depth. a**, for individual PREs, **b**, for all outputs binned, for ΔC^* C_{anth}. Numbers and colors relate

766   to regions in Extended Data Figure 1a. Dots relate to Western basin, circles to Eastern basin

767
768

Pressure [dbar]

C_{anth} residual [μmol kg^{-1}]

Pressure [db]

Residual [μmol kg^{-1}]
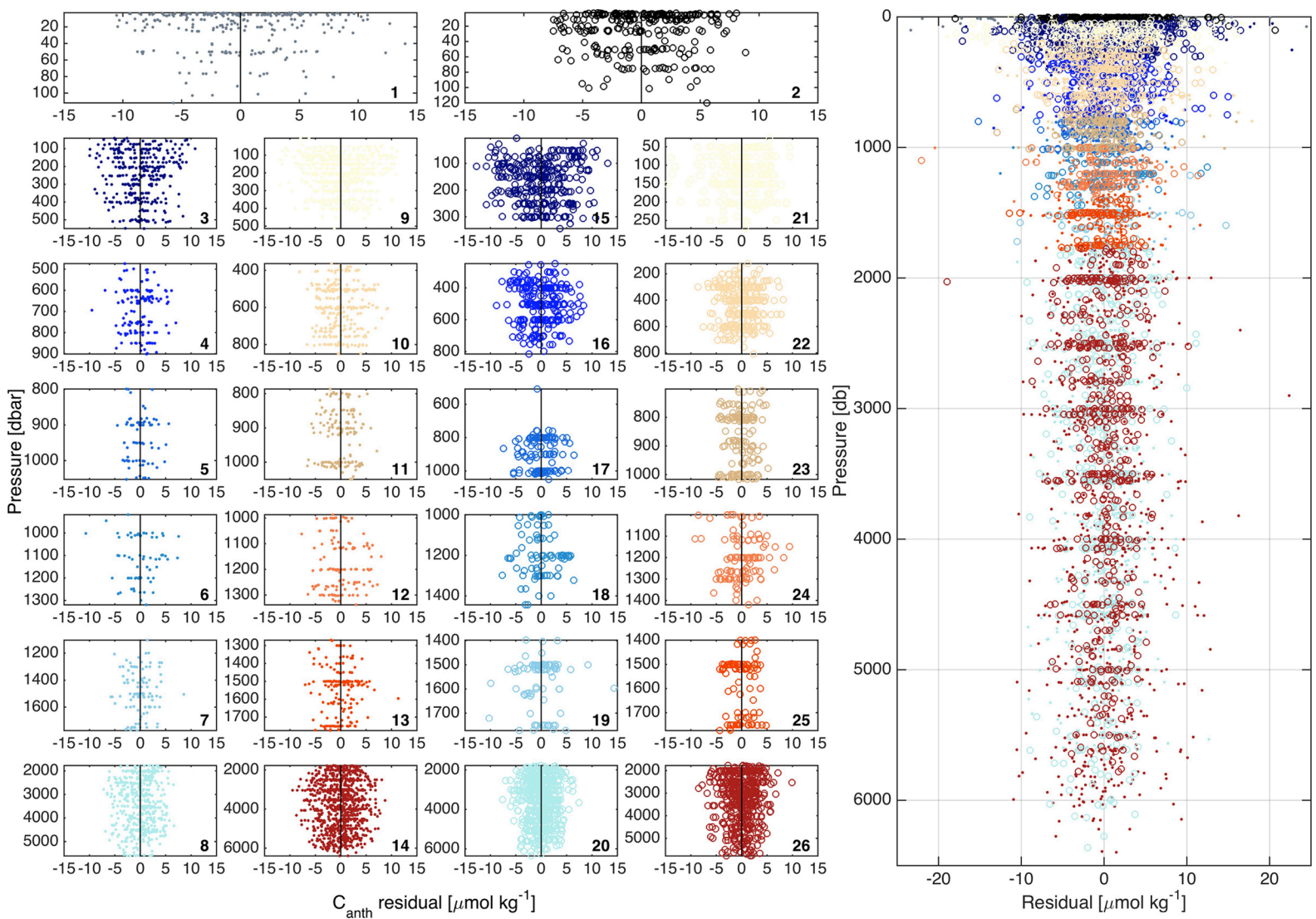
769   **Extended Data Figure 3. Bottle C_{anth} estimates versus PRE predicted C_{anth} for ΔC^* $C_{anth.}$**

770   Numbers and colors relate to regions in Extended Data Figure 1a. Black lines indicate unity. Red

771   lines indicate linear least squares fit of bottle estimates versus predicted. Dots relate to Western

772   basin, circles to Eastern basin

773

774

MLR Predicted C$_{anth}$ [μmol kg^{-1}]

Bottle C$_{anth}$ [μmol kg^{-1}]
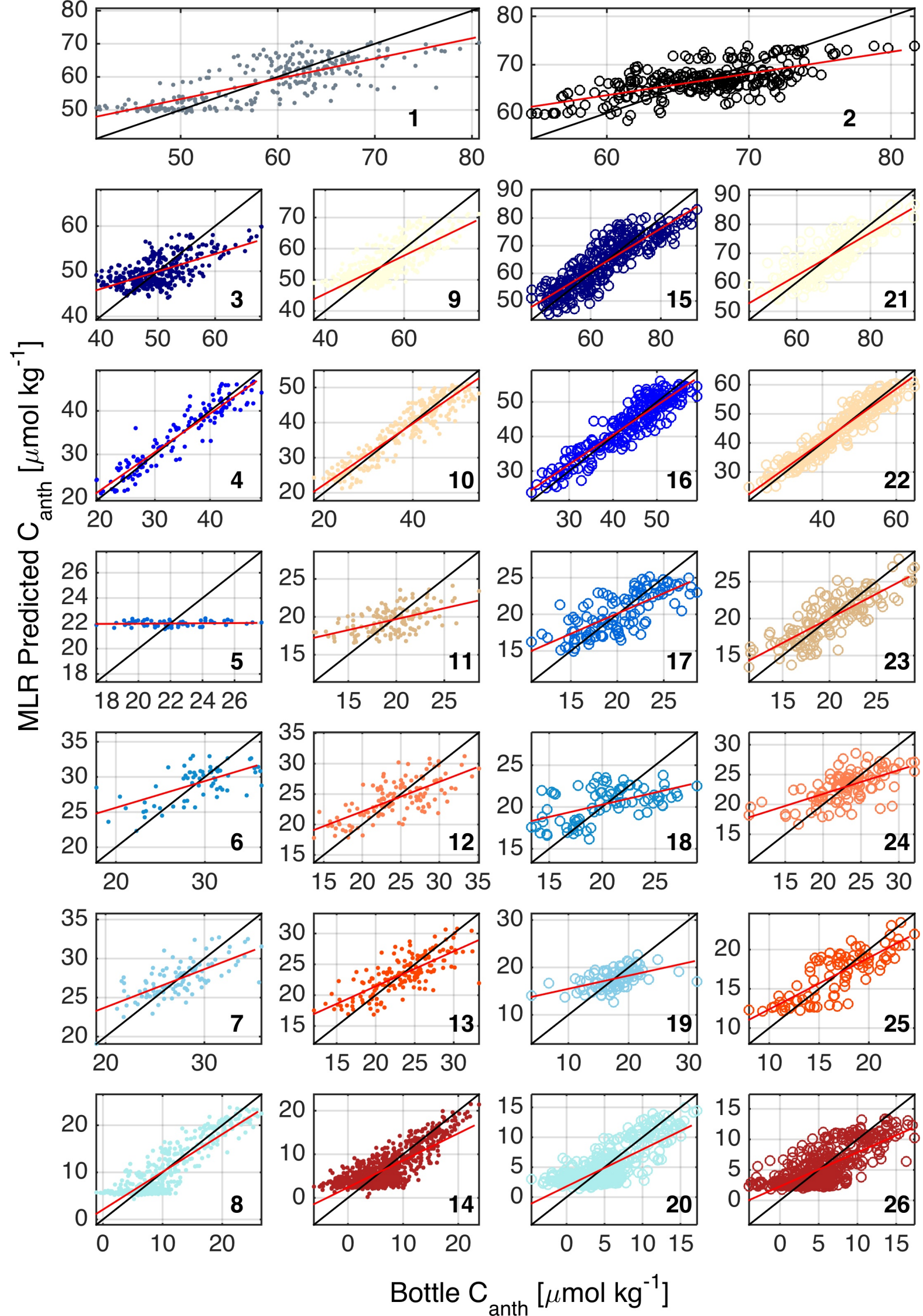
775   **Extended Data Figure 4. Schematic of Pre-industrial DisEquilibrium (SPIDEr) mixed layer**

776   **C_{anth} calculation.** Blue colour implies pre-industrial era, yellow colour implies modern era.

777   Numbers on left refer to explanations in Methods text.

778
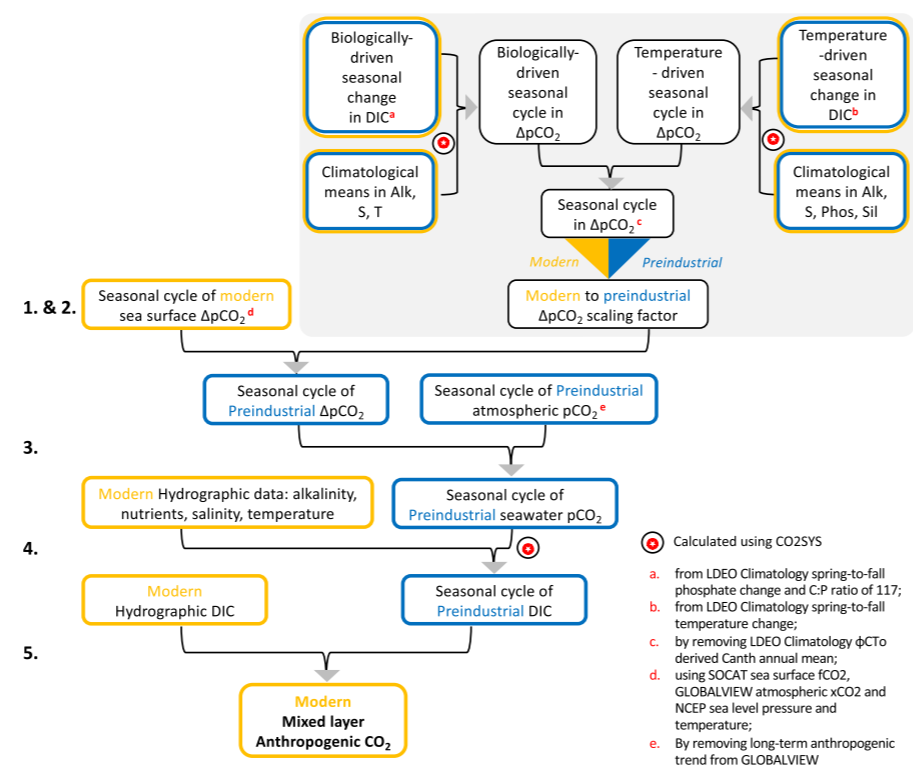
779

Biologically-driven seasonal change in DIC[a]

Biologically-driven seasonal cycle in ΔpCO_2

Temperature-driven seasonal cycle in ΔpCO_2

Temperature-driven seasonal change in DIC[b]

Climatological means in Alk, S, T

Seasonal cycle in ΔpCO_2[c]

Climatological means in Alk, S, Phos, Sil

Modern   *Preindustrial*

1. & 2.

Seasonal cycle of modern sea surface ΔpCO_2[d]

Modern to preindustrial ΔpCO_2 scaling factor

Seasonal cycle of Preindustrial ΔpCO_2

Seasonal cycle of Preindustrial atmospheric pCO_2[e]

3.

Modern Hydrographic data: alkalinity, nutrients, salinity, temperature

Seasonal cycle of Preindustrial seawater pCO_2

4.

Modern Hydrographic DIC

Seasonal cycle of Preindustrial DIC

5.

Modern **Mixed layer Anthropogenic CO_2**

Calculated using CO2SYS

a. from LDEO Climatology spring-to-fall phosphate change and C:P ratio of 117;
b. from LDEO Climatology spring-to-fall temperature change;
c. by removing LDEO Climatology ϕCTo derived Canth annual mean;
d. using SOCAT sea surface fCO2, GLOBALVIEW atmospheric xCO2 and NCEP sea level pressure and temperature;
e. By removing long-term anthropogenic trend from GLOBALVIEW

780   **Extended Data Figure 5. Variability in predicted surface layer C$_{anth}$.** For 2009 at 62.375°W

781   with C$_{anth}$ plotted against **a**, pressure, **b**, neutral density and **c**, potential temperature. Color refers

782   to time of year.

783
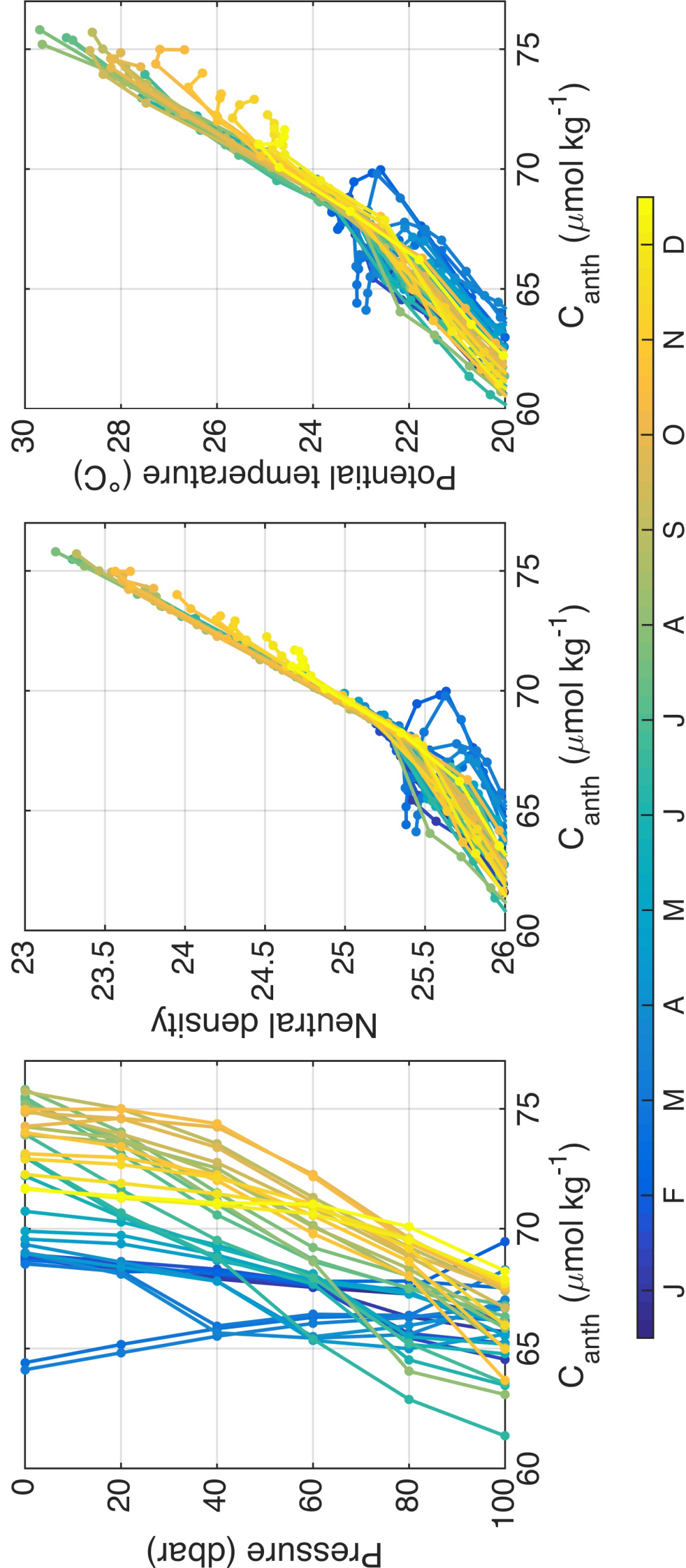
786   **Extended Data Figure 6. C_{anth} transports across Florida Straits and 26.5°N. a**, transport-

787   weighted C_{anth} transports and volume transports for Florida Straits in 2004, 2010 and 2012. Lines

788   are linear predictive fits. TTD has no data for 2012. **b**, C_{anth} transports across 26.5°N on ten-day

789   (thin lines) and 3-month filtered (thick lines) timescales for 2004.3-2012.8 for four C_{anth}

790   calculation methods with 2004-2012 averages and standard deviation.

791

792
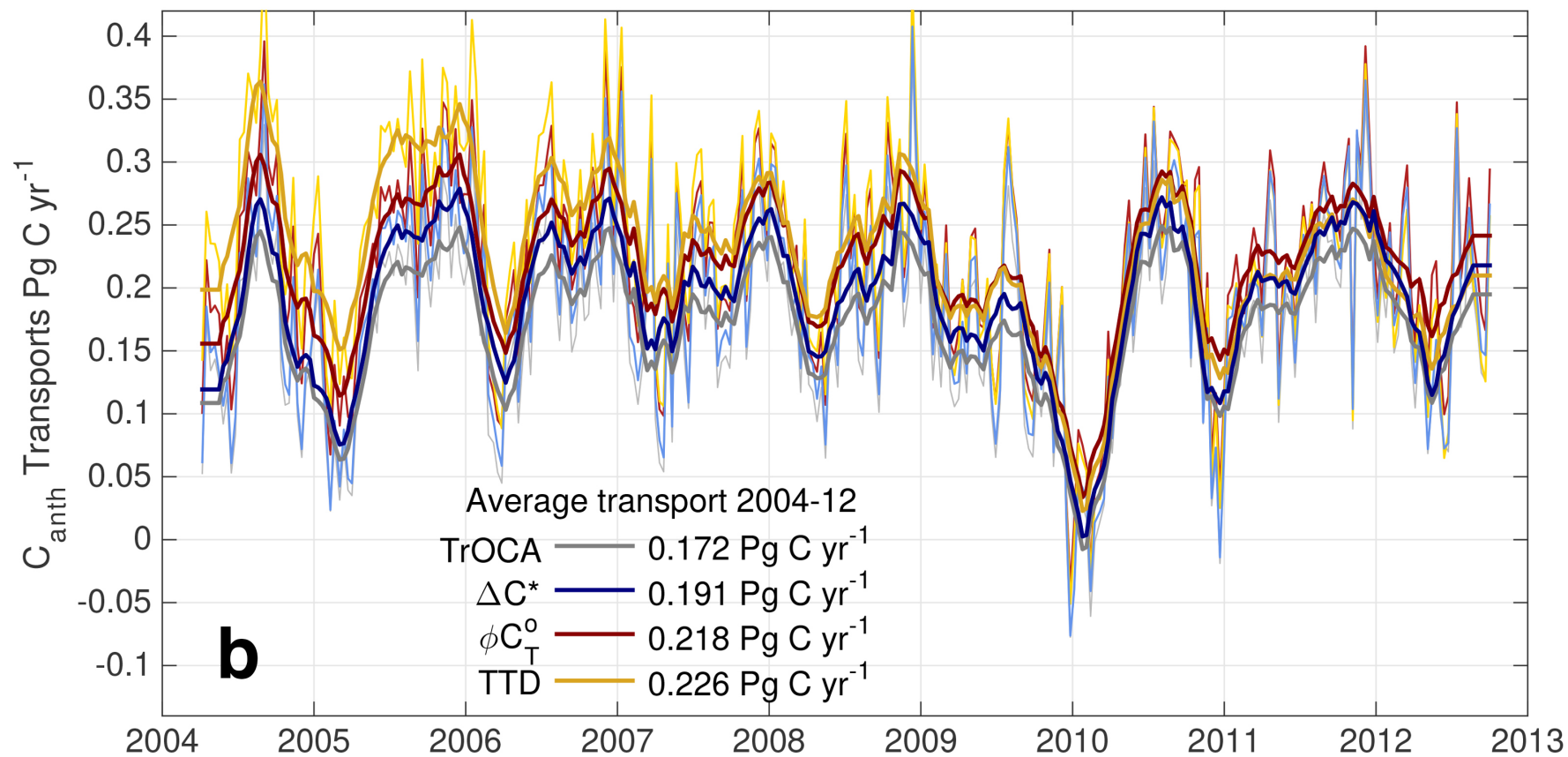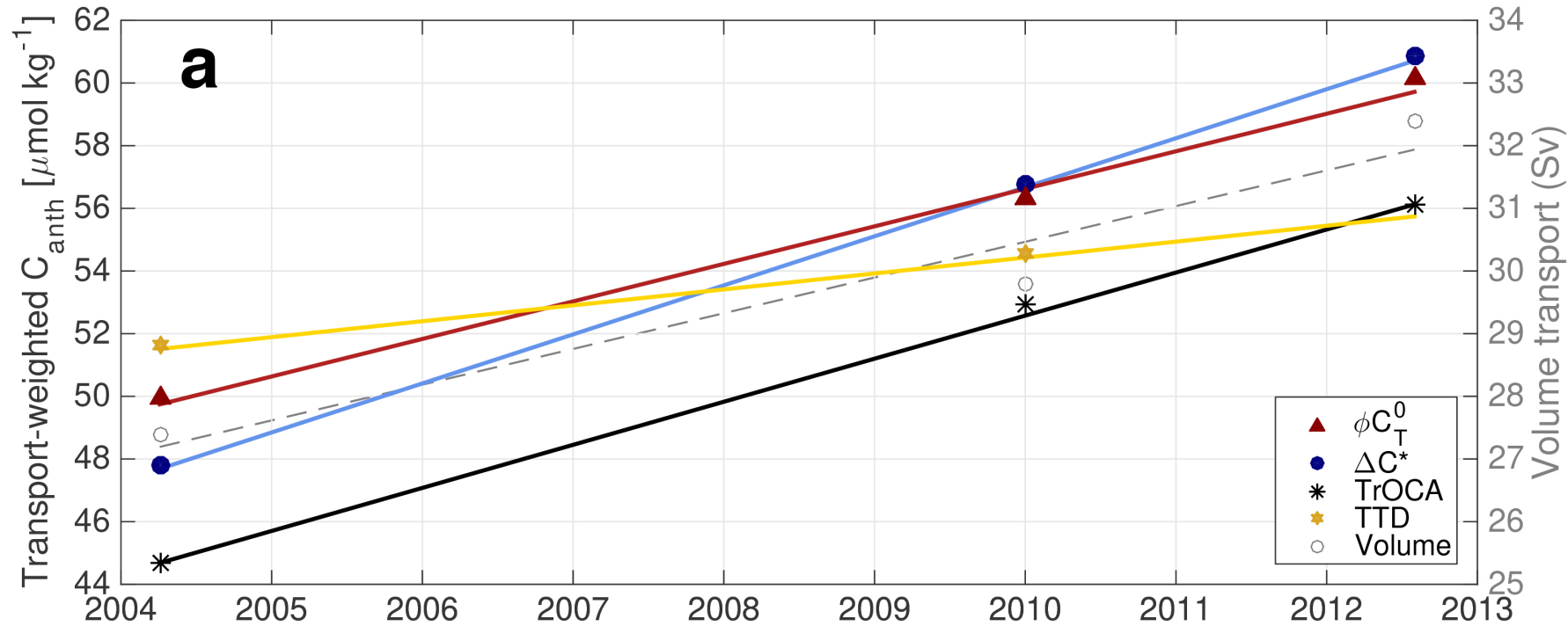
793   **Extended Data Figure 7. Application of C_{anth} transport calculation methodology to model**

794   **outputs.** Anthropogenic carbon transports (a,c) and their residual from the model truth (b,d) for

795   1980-2100 (a,b) and 2004-2013 (c,d) for five unique applications of the PRE methodology

796   applied to 1° NEMO-MEDUSA model outputs. Legend lists colour schemes of model truth, and

797   different modifications of PRE methodology applied. For conversion of carbon transports, 660

798   kmol s^{-1} = 0.25 PgC yr^{-1}.

799
800

NEMO-MEDUSA model outputs

Anthropogenic carbon transports

Residuals from model truth
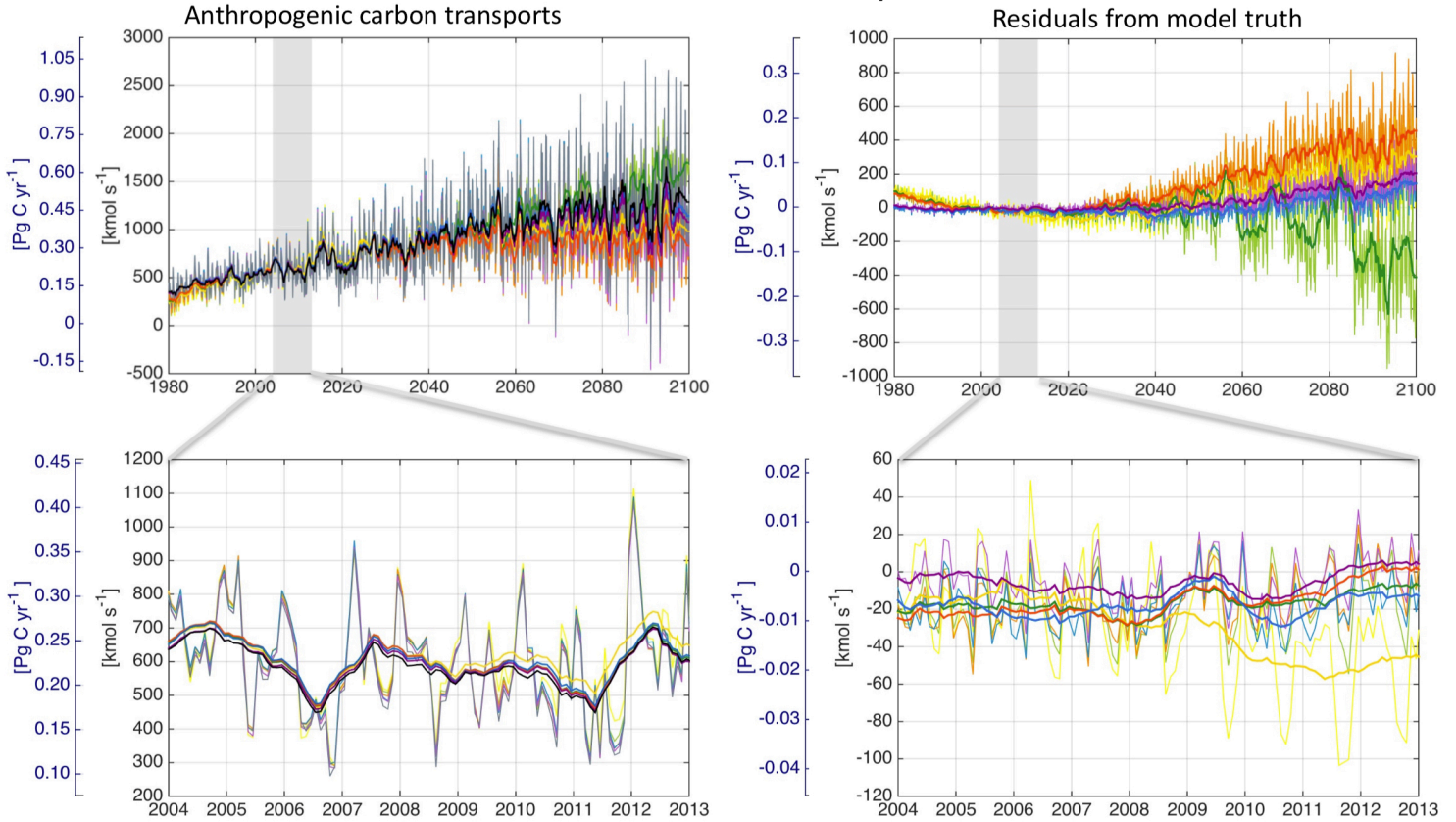
	Number of PRE regions	PRE boundaries optimised to hydrography of:	Months of data for each input year (1992, 1998, 2004, 2010, 2011) for PRE training	Trend in ΔC_{anth}	Vertical data resolution
	30	Observations	1	Linear	20 data points
	55	Model	1	Linear	20 data points
	55	Model	12	Linear	20 data points
	55	Model	12	Non-linear	20 data points
	55	Model	12	Non-linear	64 data points
	Model Truth				

801 **Extended Data Figure 8. Application of back-calculation C_{anth} methodology to model**

802 **outputs.** Top: Anthropogenic carbon transports for 1980-2100 for 1. application of ΔC^* C_{anth}

803 calculation method to 1° NEMO-MEDUSA model outputs combined with model velocity fields,

804 and 2. model truth. Bottom, as for top but for 2004-2013. Monthly values and 12-month running

805 mean shown for both. For conversion of carbon transports, 660 kmol s^{-1} = 0.25 PgC yr^{-1}.

806
807
808

Anthropogenic carbon transports - model truth & ΔC^* estimate
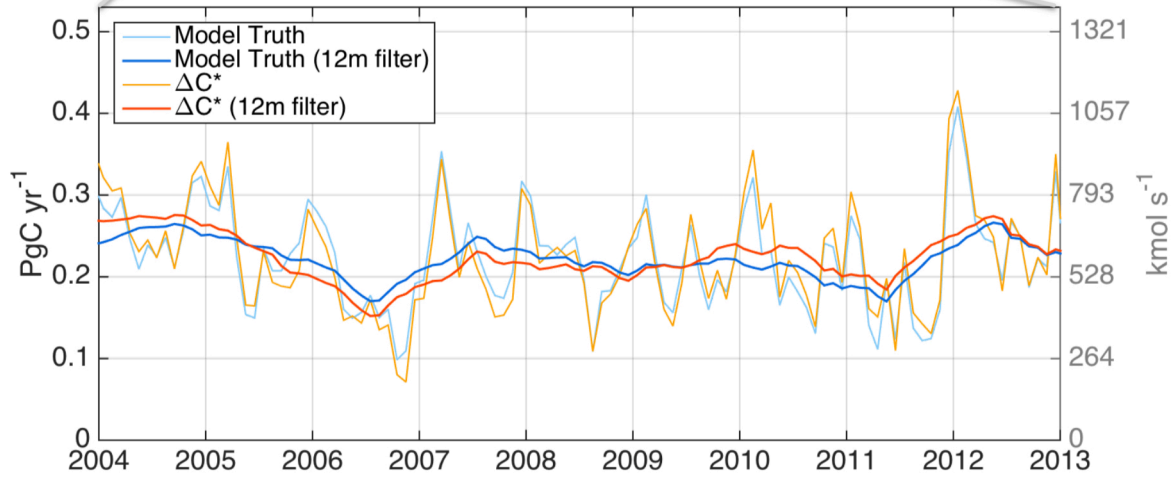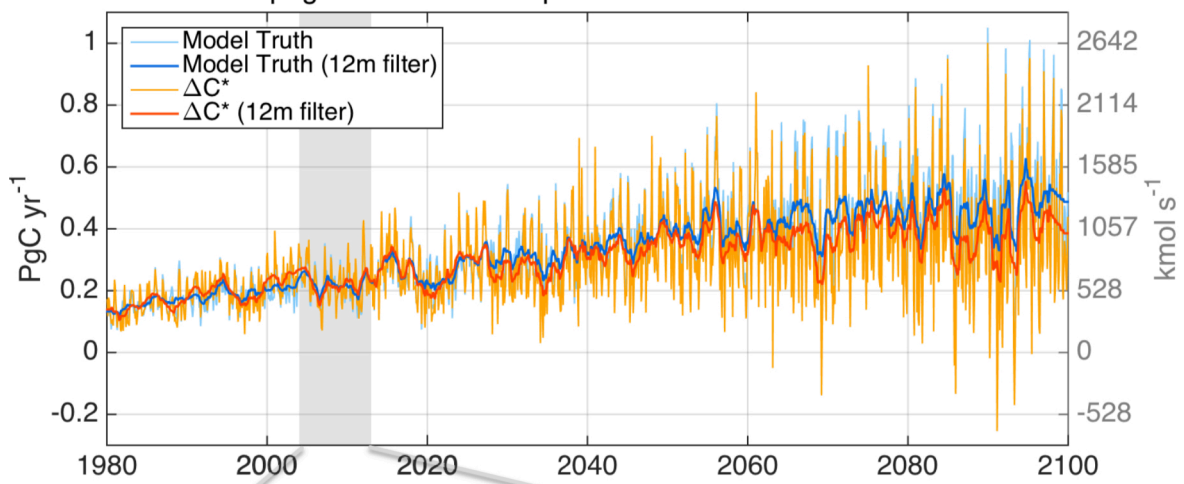
Region	Water mass	Bin	a (x 10^{-6})	b (x 10^{-6})	c (x 10^{-9})	d (x 10^{-8})	y^0 (x 10^{-3})
Surface to bottom of mixed layer	78°W to 46°W	1	1.009	-2.724	-12.080	62.337	0.175
	46°W to 10°W	2	2.304	5.147	12.787	24.827	-0.171
	78°W to 70°W	3	2.624	11.795	39.434	11.059	-0.436
Bottom of mixed layer to $y_n < 26.7$	70°W to 46°W	9	2.251	11.477	36.820	25.075	-0.406
	46°W to 30°W	15	4.245	-0.265	8.463	78.169	0.017
	30°W to 10°W	21	3.342	-3.342	-64.403	4.573	0.137
	78°W to 70°W	4	8.198	-36.086	-5.613	1.910	1.226
$26.7 < y_n < 27.4$	70°W to 46°W	10	9.094	-40.930	-5.046	11.123	1.394
	46°W to 30°W	16	9.854	-48.630	-13.785	20.383	1.670
	30°W to 10°W	22	7.961	-25.158	-4.511	19.469	0.848
	78°W to 70°W	5	-0.527	9.269	0.427	-6.383	-0.305
$27.4 < y_n < 27.65$	70°W to 46°W	11	-1.623	32.461	-6.910	-11.214	-1.107
	46°W to 30°W	17	2.193	14.796	6.004	7.694	-0.520
	30°W to 10°W	23	-2.222	44.411	-16.506	3.723	-1.511
$27.65 < y_n < 27.85$	78°W to 70°W	6	-9.157	104.091	-10.603	-49.165	-3.594
	70°W to 46°W	12	-7.517	38.737	-11.749	-23.973	-1.292
	46°W to 30°W	18	-6.154	27.031	-5.122	11.632	-0.882
	30°W to 10°W	24	-9.678	84.053	-27.709	-0.336	-2.843
	78°W to 70°W	7	21.866	-176.227	11.292	3.156	6.090
$27.85 < y_n$ & Pressure <1775 dbar	70°W to 46°W	13	5.391	-57.011	-9.694	-22.221	2.000
	46°W to 30°W	19	19.227	-56.380	29.443	-14.079	1.853
	30°W to 10°W	25	0.344	22.632	-16.530	4.167	-0.754
	78°W to 70°W	8	15.312	-96.938	0.899	-8.254	3.349
Pressure > 1775 dbar	70°W to 46°W	14	18.645	-122.293	2.022	-10.631	4.220
	46°W to 30°W	20	6.856	4.438	1.541	-1.594	-0.174
	30°W to 10°W	26	8.509	-34.556	0.875	4.583	1.189

809   **Extended Data Table 1. Predictive coefficients a-d and constant y^0 from PREs for**

810   **individual bins**, according to $normC_{anth} = a*\theta + b*Sal + c*pres + d*lon + y^0$, where '$\theta$' is

811   potential temperature (°C), 'Sal' is salinity, 'pres' is pressure (dbar), and 'lon' is longitude (°E).

812   Results here are from $\Delta C^* \, C_{anth}$ outputs.

813

814

Region	Water mass		σT_{reg} (Sv)	$(C_{reg} - C_{sect})$ (µmol kg^{-1})	σCT_T (TgC yr^{-1})	σC_{reg} (µmol kg^{-1})	T_{reg} (Sv)	σCT_C (TgC yr^{-1})	σCT (TgC yr^{-1})
Surface to bottom of	78°W to 46°W	1	0.63	19.7	5	29.3	-0.97	-10	11
mixed layer	46°W to 10°W	2	0.87	31.7	10	29.2	-5.4	-58	59
	78°W to 70°W	3	5.04	27.3	51	9.5	4.2	15	53
Bottom of mixed layer	70°W to 46°W	9	4.53	33.9	57	2.9	-5.2	-5	57
to $\gamma_n < 26.7$	46°W to 30°W	15	1.08	38.3	15	5.1	-2.5	-5	16
	30°W to 10°W	21	0.39	43.6	6	3.1	-1.3	-1	7
	78°W to 70°W	4	2.59	12.7	12	13.2	2.3	11	17
$26.7 < \gamma_n < 27.4$	70°W to 46°W	10	2.91	20.1	22	8.3	-2.2	-7	23
	46°W to 30°W	16	1.46	23.3	13	8.7	-2.3	-8	15
	30°W to 10°W	22	1.77	24.6	16	9.7	-3.6	-13	21
	78°W to 70°W	5	0.61	3.8	1	0.5	0.53	0	1
$27.4 < \gamma_n < 27.65$	70°W to 46°W	11	0.75	2.4	1	1.2	-0.13	0	1
	46°W to 30°W	17	0.56	2.9	1	2.7	-0.13	0	1
	30°W to 10°W	23	0.57	3.4	1	2.1	-0.26	0	1
$27.65 < \gamma_n < 27.85$	78°W to 70°W	6	0.48	9.8	2	2.7	0.17	0	2
	70°W to 46°W	12	0.60	5.1	1	2.8	-0.37	0	1
	46°W to 30°W	18	0.50	0.9	0	1.8	-0.21	0	0
	30°W to 10°W	24	0.42	4.6	1	2.0	-0.48	0	1
	78°W to 70°W	7	0.55	0.0	2	0.0	-0.62	0	2
$27.85 < \gamma_n$ &	70°W to 46°W	13	0.38	4.5	1	3.2	-1.35	-2	2
Pressure <1775 dbar	46°W to 30°W	19	0.23	0.6	0	2.5	-0.68	-1	1
	30°W to 10°W	25	0.18	-0.7	0	3.0	-0.71	-1	1
	78°W to 70°W	8	0.92	0	-3	0.0	-1.7	-3	4
Pressure > 1775 dbar	70°W to 46°W	14	1.89	-11.5	-8	4.5	-5.2	-9	12
	46°W to 30°W	20	1.09	-14.8	-6	3.2	-3.6	-4	7
	30°W to 10°W	26	0.86	-14.2	-4	3.2	-3.1	-4	6
Bering Strait			0.20	27.0	2	6.2	0.80	2	3
Ekman			0.20	47.7	4	6.3	3.50	6	7
Florida Strait			0.99	25.9	10	6.2	31.58	72	72
C_{anth} estimate & ΔC_{anth}									37

Total uncertainty in individual 10-day C_{anth} transport estimates	0.135 Pg C yr^{-1}
Total uncertainty in annual average C_{anth} transport	0.039 Pg C yr^{-1}
Total uncertainty in average C_{anth} transport for full time-series	0.013 Pg C yr^{-1}

815   **Extended Data Table 2. C_{anth} transport uncertainty estimates.** Key to column headings:

816   σT_{reg}, uncertainty in regional transport; $C_{\_reg}$, regional C_{anth} average; $C_{\_sect}$, section C_{anth} average;

817   $(C_{\_reg} - C_{\_sect})$, regional C_{anth} anomaly; σCT_T, C_{anth} transport transport-related uncertainty; $\sigma C_{\_reg}$,

818   uncertainty in regional C_{anth} average; T_{reg}, regional transport; σCT_C, uncertainty in C_{anth} transport

819   due to uncertainty in C_{anth}; σCT, total uncertainty. Section-averaged C_{anth} (C_{sect}) is estimated as

820   18.8×10^{-6} kmol m^{-3} (~18 μmol kg^{-1}). Combining in quadrature, each ten-day estimate of C_{anth}

821   transport has an uncertainty of 0.135 PgC yr^{-1}. Assuming that there are 12 independent estimates

822   in the year then the uncertainty on the annual average C_{anth} transport is 0.135 PgC yr$^{-1}/(12)^{1/2} =$

823   0.039 PgC yr^{-1}. Assuming there are 102 independent estimates across the full 8.5-year time series

824   then the uncertainty on the full time series average C_{anth} transport is 0.135 PgC yr$^{-1}/(102)^{1/2} =$

825   0.013 PgC yr^{-1}.

826
827